Nano Research

ISSN 1998-0124 CN 11-5974/O4
https://doi.org/10.26599/NR.2026.94908813

Research Article

A bioinspired suction-activated nanofibrous patch for adaptive skin adhesion and enhanced transdermal delivery

Minjin Kim[1,§], Minwoo Song[1,§], Hyoung-Ki Park[1,2,§], Gui Won Hwang[1], Jihun Son[1], Changrok Park[1], Gyun Ro Kang[1], Changhyun Pang[1,3](✉)

[1] School of Chemical Engineering Sungkyunkwan University (SKKU), 2066 Seobu-ro, Jangan-gu, Suwon 16419, Republic of Korea

[2] Mimetics Co., Ltd, 2066 Seobu-ro, Jangan-gu, Suwon 16419, Republic of Korea

[3] Samsung Advanced Institute for Health Science & Technology (SAIHST) Sungkyunkwan University (SKKU), Seoul, 06351, Republic of Korea

[§] Minjin Kim, Minwoo Song, and Hyoung-Ki Park contributed equally to this work.

Nano Res., **Just Accepted Manuscript** • https://doi.org/10.26599/NR.2026.94908813

https://www.sciopen.com/journal/1998-0124 on May. 6, 2026

Just Accepted

TABLE OF CONTENTS (TOC)

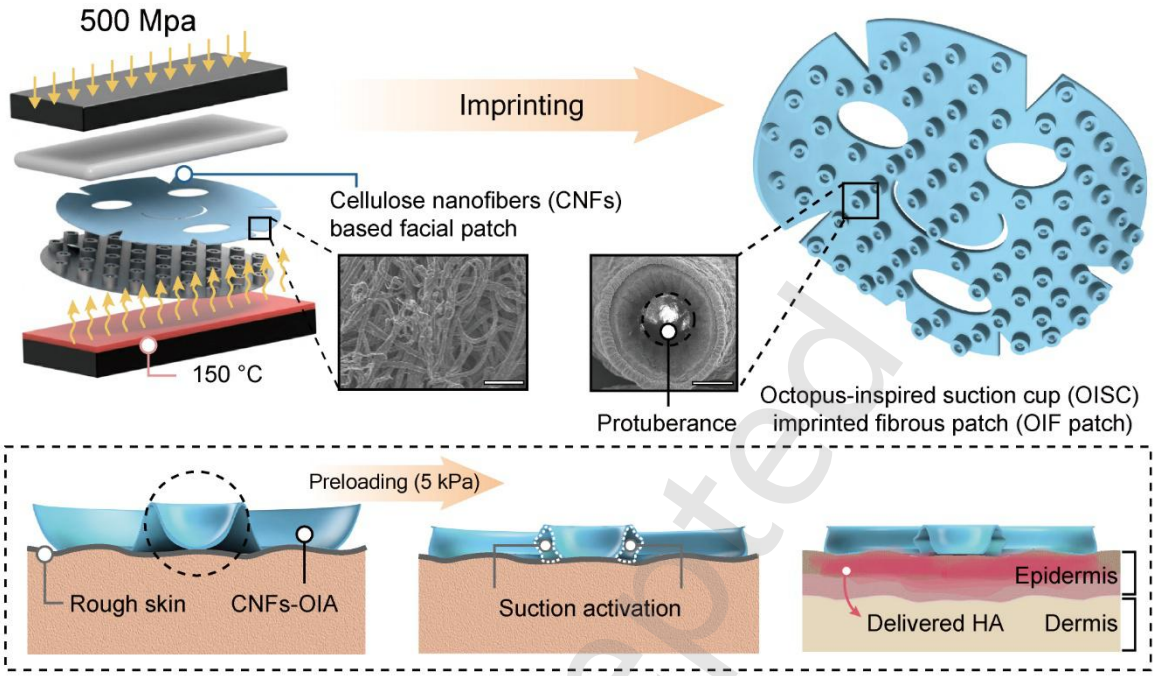

A cellulose nanofiber based transdermal patch (OIF patch) with an octopus-inspired suction cup (OISC) enables adaptive skin adhesion and enhanced active ingredient delivery under dynamic deformation. Fabricated via a simple imprinting process, OIF patch maintains robust adhesion and up to 350% higher delivery depth even under severe bending and diverse skin conditions.

Nano Research

Open Access

Research Article

A bioinspired suction-activated nanofibrous patch for adaptive skin adhesion and enhanced transdermal delivery

Minjin Kim[1, §], Minwoo Song[1, §], Hyoung-Ki Park[1,2 §], Gui Won Hwang[1], Jihun Son[1], Changrok Park[1], Gyun Ro Kang[1], and Changhyun Pang[1,3] ✉

[1] *School of Chemical Engineering Sungkyunkwan University (SKKU), 2066 Seobu-ro, Jangan-gu, Suwon 16419, Republic of Korea*

[2] *Mimetics Co., Ltd, 2066 Seobu-ro, Jangan-gu, Suwon 16419, Republic of Korea*

[3] *Samsung Advanced Institute for Health Science & Technology (SAIHST) Sungkyunkwan University (SKKU), Seoul, 06351, Republic of Korea*

[§] *Minjin Kim, Minwoo Song, and Hyoung-Ki Park contributed equally to this work.*

Received: 25 February 2026; **Revised:** 16 April 2026; **Accepted:** 6 May 2026

✉ Address correspondence to chpang@skku.edu

Cite this article: *Nano Research*, 2026, 19, 94908813 https://doi.org/10.26599/NR.2026.94908813

ABSTRACT: Transdermal delivery offers a user-friendly and minimally invasive route to overcome limitations of conventional oral and injectable methods. Cellulose nanofibers (CNFs)-based skin-adhesive patches have emerged as promising platforms to enhance transdermal delivery efficiency owing to their biocompatibility and porous fibrous networks. However, the fabrication of CNFs-based patches that can withstand high-viscosity solutions while maintaining adaptive adhesion under deforming skin conditions remains challenging. Moreover, existing strategies to impart functionality often rely on complex and precision-intensive fabricating processes. Here, we present a CNFs-based transdermal patch (OIF patch) incorporating an octopus-inspired suction cup (OISC), fabricated via a straightforward imprinting process. Under optimized fabrication conditions (150 °C and 500 MPa), OIF patch maintains structural integrity without thermal degradation and demonstrates enhanced robustness in highly viscous environments. The imprinted OISC induces deformation-driven negative pressure, enabling intimate and adaptive skin adhesion even under bending deformation (up to 90°). Consequently, OIF patch demonstrates robust adhesion across diverse skin conditions and achieves up to a 350% enhancement in transdermal delivery depth compared to flat fibrous. Clinical evaluations further confirm improvements in multiple skin parameters, underscoring the translational potential of OIF patch. This work establishes a scalable and adaptable CNFs-based platform for reliable transdermal delivery under user-induced dynamic conditions.

KEYWORDS: nanofiber, biomimetics, adhesion, cellulose, transdermal drug delivery

1 Introduction

The skin is the largest organ of the human body, and transdermal delivery has emerged as a promising alternative to conventional oral and injectable administration routes by overcoming their inherent limitations [1]. Transdermal delivery enables the minimally invasive administration of active ingredients directly to targeted sites, allowing for self-administration, improved patient compliance, and sustained or controllable release when integrated with patch-based systems [2, 3]. Despite these advantages, the skin presents a formidable barrier to molecular transport owing to its highly organized, multilayered biological architecture [4]. In particular, the stratum corneum exhibits a characteristic brick-and-mortar organization that plays a central role in restricting the permeation of exogenous molecules [1, 5]. In addition to its structural characteristic, the skin is continuously subjected to dynamic mechanical deformations, such as bending and stretching, arising from routine body movements. These structural and mechanical constraints critically limit molecular diffusion and penetration, thereby significantly reducing transdermal delivery efficiency [5]. To address these challenges, considerable efforts have been devoted to the development of skin adhesive patches designed to enhance mechanical conformability at the patch–skin interface and thereby improve transdermal delivery [6, 7]. Such strategies are particularly attractive because they can preserve adaptive adhesion even under dynamic skin deformation, ensuring continuity of the delivery pathway. However, many existing approaches rely on complex architectures incorporating drug reservoirs, adhesive layers, and electrically or mechanically driven components, which inevitably increase fabrication complexity and often require additional user manipulation or external power sources [8-12]. As a result, existing patch-based systems remain limited in terms of accessibility and broad applicability in real-world user environments.

Nanofibers are composed of continuous fibrous networks with diameters ranging from several tens to hundreds of nanometers [13]. They have been extensively explored in a wide range of biomedical applications, including transdermal delivery, wound healing, artificial skin, and tissue engineering [14-16]. The broad applicability of nanofibers arises from their high specific surface area, interconnected porous architecture, and excellent mechanical conformability [17]. Such structural attributes facilitate efficient loading and controlled release of active ingredients [18]. Accordingly, nanofibers have emerged as a promising material platform for transdermal delivery related applications [19, 20]. Depending on their origin, nanofibers can be classified into plant-derived polysaccharide-based materials, such as cellulose, and animal-derived protein-based materials, including silk fibroin and gelatin [21-23]. Each class exhibits distinct physicochemical properties governed by its molecular structure and chemical composition [21, 24]. These differences lead to variations in mechanical stability, hydrophilicity, biodegradability, and biological interaction behavior [21, 25]. However, gelatin-based nanofibers are highly sensitive to moisture and temperature fluctuations [22, 26, 27]. This sensitivity compromises their structural stability

under the wet conditions that are intrinsic to transdermal delivery. In contrast, silk fibroin can achieve superior mechanical strength and durability through the formation of β-sheet crystalline domains [23]. On the other hand, the crystallization and fabrication of silk fibroin generally require a high level of precision and are often difficult to control in a reproducible manner [28-30]. In addition, the use of organic solvents such as formic acid during processing raises concerns regarding potential skin compatibility in translational applications [31]. Moreover, the intrinsic physicochemical properties of silk fibroin can induce selective interactions with active ingredients [31]. Such interactions may impede molecular diffusion within the matrix and adversely affect release behavior [32].

By contrast, cellulose-based nanofibers (CNFs) offer several advantages arising from the intrinsic chemical stability of polysaccharides and their relatively low biological reactivity [33, 34]. These properties result in minimal skin irritation and enable the maintenance of structural integrity during long-term application [35, 36]. Furthermore, CNFs exhibit enhanced delivery efficiency across a broad range of active ingredients with diverse physicochemical properties, showing minimal dependence on molecular hydrophilicity or hydrophobicity [37, 38]. Consequently, CNFs demonstrate versatility in transdermal delivery while maintaining relatively uniform and predictable release characteristics [39, 40]. Nevertheless, several limitations remain in the use of CNFs for transdermal delivery. Prolonged exposure to high-viscosity liquid formulations can induce localized deformation or partial collapse of the fibrous network [41, 42]. This structural instability may reduce capillary forces at the fiber–skin interface, thereby promoting patch detachment and diminishing delivery efficiency [43-45]. These observations indicate that the intrinsic properties of nanofibers alone are insufficient to simultaneously ensure robust skin adhesion and stable delivery performance. Although reproducible electrospinning techniques or structural/material modification strategies have been proposed to enhance the functionality of nanofibers, [15, 46, 47] maximizing adaptive skin adhesion of nanofiber-based materials under dynamically deforming conditions through structural and material optimization remains a challenge. The introduction of skin-conformal adhesive architectures represents a potential strategy to mitigate these issues. However, the fine fiber diameters and high porosity of nanofiber networks limit structural reproducibility during shaping and processing. This limitation becomes particularly pronounced in high-viscosity environments, where weakened inter-fiber interactions can lead to localized deformation and structural failure [41, 42]. Therefore, there is a compelling need for transdermal delivery platforms that preserve the intrinsic physicochemical advantages of nanofibers while enabling adaptive and sustained interfacial contact with the skin.

Here, we present an octopus-inspired suction cup (OISC) imprinted fibrous patch (OIF patch), fabricated via a simple imprinting process, which enables consistent transdermal delivery even under dynamic skin deformation (bending angle up to 90°). CNFs soften at the imprinting temperature (150 °C), enabling highly precise patterning during the process while preserving structural integrity even under

exposure to highly viscous liquids (up to 10,000 Pa·s). At an imprinting pressure of 500 MPa, the OISC exhibits deformation-induced negative pressure, contributing to enhanced and adaptive skin adhesion. Consequently, OIF patch demonstrates robust adhesion on dry, extremely dry, and wounded skin surfaces. This interfacial stability enables consistent transdermal delivery of fluorescent particles, even under severe bending deformation up to 90°. The therapeutic potential of OIF patch was further validated through clinical evaluations, demonstrating improvements in multiple skin parameters, including roughness, fine lines, and pore characteristics. Owing to its simple manufacturing process, adaptability to skin deformation, and user-friendly design, OIF patch represents a practical and scalable platform for advanced transdermal delivery applications.

2 Experimental

2.1 Materials

Biodegradable CNFs–based facial mask sheets were obtained from Mimetics Co., Ltd. and used as the base substrates for imprinting the OISC. Hyaluronic acid (HA, 5 kDa, HAworks) and phosphate-buffered saline (PBS, Sigma-Aldrich) were purchased and used as received. HA solutions were prepared at designated viscosities by adjusting the concentration in PBS.

2.2 Methods

2.2.1 Fabrication of the OIF patch

A master mold was designed using three-dimensional computer-aided design software (Autodesk Fusion 360, Autodesk Inc.) and fabricated to produce a stainless steel (SUS) mold featuring a spacing ratio of 1/3, a diameter of 3 mm, and a height of 1.5 mm. For OIF patch fabrication, the SUS mold, CNFs sheet, and an elastic damper (Ecoflex 0050, Smooth-On, Inc.) were sequentially assembled and placed into a pneumatic press (LISOTEK, Korea). The imprinting process was conducted for a fixed duration of 30 min while systematically varying the processing temperature (25–200 °C) and applied pressure (100–500 MPa).

2.2.2 Dynamic mechanical analysis of the CNFs

The temperature-dependent viscoelastic behavior of CNFs samples was evaluated using a dynamic mechanical analyzer (DMA7100, Hitachi, Japan). Dynamic mechanical analysis was performed to determine the storage modulus (E′) and loss modulus (E″) of the CNFs as a function of temperature.

2.2.3 Properties according to concentrations of HA

HA powder (5 kDa, HAworks, USA) was dissolved in phosphate-buffered saline (pH 7.4, Sigma-Aldrich, Germany) to prepare solutions with concentrations of 1, 5, 10, and 15 wt%. The mixtures were vortexed for 5 min and subsequently centrifuged at 3000 rpm for 10 min to ensure homogeneous dispersion. The

viscosities of HA solutions prepared at identical volumes were measured using a rheometer (ARES-G2, TA Instruments, USA).

2.2.4 Structural maintenance analysis depending on HA concentration

The structural integrity of OIF patch under different HA concentrations was evaluated through cross-sectional imaging. OIF patch samples fabricated at the optimized temperature of 150 °C were immersed in HA solutions (0, 10, 15 wt%) for 1 min. Cross-sectional images were acquired using a Digibird optical system (MICRO B2B, Korea). Structural retention was quantified using ImageJ software by defining the initial structure height as h_0 and the post-immersion height as h. The degree of structural maintenance was calculated as ($h / h_0 \times 100$) from 10 randomly selected locations.

2.2.5 FEM simulation

Finite element method (FEM) simulations were performed using COMSOL Multiphysics (version 6.2a, license number 5094592, Altsoft, South Korea) to analyze the structural behavior of OIF patch. A two-dimensional model incorporated the dimensions of each OIF patch unit defined by the applied imprinting pressure. The geometry was meshed using tetrahedral elements with mesh sizes ranging from 0.0057 to 0.014 mm. Poisson's ratio was set to 0.49, and all materials were assumed to be linear elastic. A pseudostatic analysis was employed for simulation.

2.2.6 Adhesion performance analysis on porcine skin

Fresh porcine skin obtained from a local butcher in Jidong, Korea was used on the day of purchase to minimize deformation. Adhesion measurements were conducted at 25 °C using a custom-built testing system (Neo-Plus, Korea). Samples were mounted onto a jig connected to a force sensor and brought into contact with the porcine skin surface. A preload of 5 kPa was applied for 5 s prior to detachment. Normal adhesion tests were repeated at least 10 times, and mean values were reported. For shear adhesion tests, samples were detached at a constant velocity of approximately 0.1 mm/s, with measurements performed at least five times.

2.2.7 Fabrication of microneedles

Microneedles were fabricated using a hyaluronic acid (HA)-based casting process. A 5 wt% HA solution was prepared and poured into a microneedle master mold (Micropoint Technologies Pte Ltd, Singapore). The HA-filled mold was then vortexed for 5 min and centrifuged at 3000 r min^{-1} for 10 min to promote uniform filling of the mold cavities. Subsequently, degassing was performed to remove trapped air bubbles, and the mold was cured at 37 °C for 6 h to complete microneedles fabrication.

2.2.8 FTIR analysis

OIF patch applied porcine skin samples and untreated porcine skin samples were sectioned into 1 × 1 cm² areas, and residual components were analyzed using Fourier transform infrared (FTIR) spectroscopy.

2.2.9 Transepidermal water loss (TEWL) measurement

Transepidermal water loss (TEWL) was measured at 25 °C and 25% relative humidity using a closed-chamber WVER (water vapor evaporation rate) measurement device (AquaFlux, BioX). During measurement, the probe was firmly sealed against the forearm of each subject (n = 4), and WVER values were recorded over approximately 60 s. Baseline TEWL values were obtained prior to application. For post-treatment assessment, the OIF patch was applied daily for 20 min over a period of 14 days. TEWL measurements were performed after removal of residual materials following the final application.

2.2.10 Evaluation of skin irritation of the OIF patch

To assess the biocompatibility of the patch, OIF samples (2 cm × 2 cm) containing HA were applied to the forearm of each subject for 20 min. To ensure the reliability of the results, data were collected from volunteers without any known skin disorders. Skin irritation was quantitatively evaluated by analyzing erythema using ImageJ software, where the normalized intensity of the RGB channels ($\Delta I/I_{before}$) was calculated. A small cohort of healthy volunteers (n = 4) was recruited, consisting of one male and one female in their 20s and one male and one female in their 30s, with no history of specific skin conditions.

2.2.11 Analysis of transdermal delivery depth on porcine skin

Rhodamine B was incorporated into HA solutions at a mass ratio of 10:1 (HA:Rhodamine B) to enable fluorescence-based detection. Transdermal delivery depth was evaluated by varying application time, structural configuration, and HA concentration. Delivery depth of rhodamine B into porcine skin was visualized using confocal laser scanning microscopy (Leica, Germany). Quantitative depth measurements were obtained from cross-sectional images at 10 randomly selected locations using ImageJ software.

2.2.12 Analysis of skin improvement in volunteers

Skin condition changes were assessed using Antera 3D® (Miravex Limited, Ireland). Four volunteers participated in the study, and OIF patch and topical formulations were applied simultaneously to the back of the hand in a bending state for 20 minutes daily for 14 days. Considering both gender and age, a volunteer cohort was established consisting of one male and one female in their twenties, and one male and one female in their thirties, all of whom were free from specific skin disorders. The quantitative analysis was conducted using a single-blind approach to ensure objectivity. Three-dimensional skin

images were acquired before treatment and on days 1–14 after application. Images were collected immediately after residue removal. Quantitative analysis was performed using the Antera software by selecting four randomly chosen circular regions (5 mm diameter) per application site and averaging the results. Skin improvement rates were calculated using the equation $(X_0 - X_i) / X_0 \times 100$. Institutional Review Board approval was obtained (IRB No. SKKU 2024-08-061).

2.2.13 Quantification of fine lines

Fine line characteristics were quantified using three-dimensional skin images obtained from Antera 3D®. Parameters including total fine line length, average fine line width, and the number of individual fine lines were measured within selected regions to enable detailed evaluation of skin condition improvement.

2.2.14 Quantification of pores

Pore morphology was analyzed using Antera 3D® imaging. The mean pore area (mm²), maximum pore depth, and total pore count were quantified within designated regions. These parameters were used to comprehensively assess pore-related skin improvements.

3 Results and discussion

3.1 Design and Characterization of the OIF patch

To achieve stable transdermal delivery regardless of dynamic skin deformation, we developed OISC imprinted CNFs based fibrous patch (OIF patch). As illustrated in Fig. 1(a), the OIF patch was fabricated through an optimized thermal imprinting process. Leveraging the high mechanical strength and thermal stability of CNFs, we successfully fabricated a facial patch with a precisely defined OISC pattern by subjecting the CNFs film to a pressure of 500 MPa at 150 °C (Fig. 1(b)). The OISC, the core structure of this patch, is inspired by the octopus' sucker, which contains an internal protuberance to facilitate adaptive adhesion even with highly irregular and rough skin surfaces (Fig. 1(c)). This structure maximizes skin adhesion by increasing the contact area and generating localized negative pressure, which induces transient deformation of the stratum corneum to facilitate efficient transdermal delivery [5, 7, 15]. The adhesion mechanism of the OIF patch is primarily driven by the activation of suction. Upon the application of a gentle preloading force (5 kPa), the OISC undergoes structural deformation that triggers a volume change within its internal chambers. This volume change generates a localized vacuum, inducing an additional suction force that ensures robust and adaptive adhesion without the need for chemical adhesives. Consequently, the OIF patch allows for the consistent transdermal delivery of active ingredients even during severe skin bending up to 90°. This performance overcomes the limitations of conventional flat patches (Flat fibrous), which fail due to void formation (Fig. 1(d)). The practical therapeutic potential of the OIF patch with hyaluronic acid (HA) was further validated through a 14-day clinical study, which

demonstrated significant improvements in key skin parameters, including a visible reduction in roughness, pores, and fine lines (Fig. 1(e)).

3.2 Temperature-Dependent Process Optimization of OIF patch

OIF patch was fabricated using a straightforward imprinting-based process, as schematically illustrated in Fig. 2(a). Briefly, a stainless-steel (SUS) master mold featuring positive relief structures was positioned on an embedded heating module, followed by sequential placement of a CNFs-based facial patch and an elastic damper to ensure uniform pressure transfer during imprinting (Fig. S1 in the ESM). This layered configuration enabled controlled thermo-mechanical deformation of the CNFs under precisely defined processing conditions. Prior to process optimization, the temperature-dependent viscoelastic properties of the CNFs were characterized by dynamic mechanical analysis (DMA) (Fig. 2(b)). At this temperature, CNFs retain their intrinsic chemical functionalities while undergoing thermal softening without entering a thermally degraded or fully rearranged state (Fig. S2). As the temperature increased, both the storage modulus (E′) and loss modulus (E″) exhibited pronounced changes beginning at approximately 100 °C, indicating significant softening of the CNFs network. Notably, a distinct peak in tan δ (E″/E′) was observed at 98.7 °C, corresponding to a transition associated with enhanced molecular mobility and viscoelastic relaxation of the CNFs. This transition temperature marks the onset of a rubbery-like state that is favorable for imprint-assisted structural deformation. To evaluate the effect of fabrication temperature on structural formation, OIF patch samples were prepared at 25, 50, 100, 150, and 200 °C under a constant imprinting pressure of 500 MPa (Fig. 2(c)). The OISC was successfully formed at 100 °C and 150 °C, where sufficient thermal softening of the CNFs matrix enabled enhanced adaptive adhesion with the mold cavities. In contrast, imprinting at 25 and 50 °C resulted in incomplete pattern formation due to the high intrinsic stiffness of the CNFs, while processing at 200 °C caused structural damage attributable to thermal degradation. Quantitative analysis of structural fidelity revealed a clear temperature dependence (Fig. 2(d)). At 150 °C, the imprinted OIF patch achieved approximately 80% of the original SUS mold height (3 mm), whereas samples fabricated at 100 °C exhibited a reduced structural replication fidelity of ≈60%. This discrepancy is attributed to differences in chain mobility, as the CNFs processed at 150 °C reside deeper within the softened, viscoelastic regime, allowing more effective replication of the mold geometry, consistent with the DMA results (Fig. 2(b)). Because CNFs-based transdermal patches are inevitably exposed to wet environments and highly viscous formulations, the structural stability of OIF patch was further evaluated under HA solutions of varying viscosity (Fig. 2(e), 2(f), and S3 in the ESM). Samples fabricated at 100 °C showed a substantial decrease in structural maintenance even under low-viscosity aqueous conditions (≈35%) and deteriorated further to ≈30% under highly viscous environments (10,000 Pa·s). In contrast, OIF patch fabricated at 150 °C retained approximately over 80% of their original structure regardless of HA viscosity. This enhanced stability is attributed to the increased viscoelastic

compliance of the CNFs network processed at 150 °C, which allows the structure to maintain its integrity under highly viscous conditions without catastrophic network rearrangement or collapse. Accordingly, 150 °C was identified as the optimal imprinting temperature for OIF patch, providing a balanced combination of structural fidelity, thermal stability, and resistance to deformation in application-relevant environments.

3.3 Optimization of Imprinting Pressure for High-Resolution OISC

The influence of imprinting pressures, ranging from 100 to 500 MPa at a constant optimized temperature of 150 °C, was investigated to ensure the high-resolution implementation of the OISC on CNFs. As shown in the representative top- and side-view images in Fig. 3(a), the structural fidelity of the OISC was highly dependent on the applied pressure. At lower pressures of 100 and 300 MPa, the CNFs exhibited insufficient imprinting, resulting in unclear patterns and low resolution. In contrast, the application of 500 MPa produced the most precise structural implementation, characterized by clearly defined protuberances. This observation was supported by quantitative analysis, which revealed that the structural fidelity significantly increased from approximately 50% at 100 MPa to over 75% at 500 MPa (Fig. 3(b)). Furthermore, the functional characteristics of the OISC with different imprinting pressure was evaluated under a 5 kPa preload. In this study, a 15 wt% HA solution exhibiting a viscosity of approximately 10,000 Pa·s was employed, and the OIF patch was prepared in a HA-loaded state. (Fig S2 in the ESM). The volumetric change rate ((V_0- V) / V_0) within the inner chamber exhibited a linear increase in correlation with the imprinting pressure, peaking at the 500 MPa pressure condition (Fig. 3(c)). This structural behavior was further elucidated through finite element method (FEM) simulations (Fig. 3(d)). The simulations compared the stress distribution and structural deformation of the OISC chambers fabricated at various pressures both before and after the application of a 5 kPa preload. For the OISC imprinted at 100 and 300 MPa, the simulations revealed limited stress concentration and minimal chamber displacement due to the initially low-profile architecture. However, the OISC fabricated at 500 MPa exhibited significant structural volume deformation, with the internal protuberance effectively interaction with the substrate interface. Such substantial volume change is essential for inducing the localized vacuum and negative pressure required to generate a strong suction force at the skin interface. We analyzed the structural characteristics of OISC and the effect of viscous liquid (HA) application on adhesion performance (Supplementary Note 1 in the ESM) [7]. Applying a 5 kPa preload causes the outer diameter (D_{out}") to expand further from its initial state D_{out}). Consequently, the total adhesive force (σ_{total}) of the CNFs containing the viscous liquid is expressed as follows:

$$\sigma_{total} = \sigma_{capillrary} + \sigma_{suction} + \sigma_{viscous} \quad (1)$$

$$\sigma_{capillrary} = \left[\frac{\pi\cdot(D"_{out}{}^2 - D"_{in}{}^2)}{4}\cdot\gamma\left(\frac{\cos\vartheta_1+\cos\vartheta_2}{h}\right) + l\cdot\gamma\right]\cdot n \quad (2)$$

$$\sigma_{suction} = \left[\frac{P_0\pi D"_{in}{}^2\epsilon}{4}\right]\cdot n \quad (3)$$

$$\sigma_{viscous} = \left[\frac{6v\cdot\eta\cdot\pi}{h}\cdot\frac{(D"_{out}{}^2 - D"_{in}{}^2)}{4}\right] \quad (4)$$

$$\sigma_{total} = \left[\frac{P_0\pi D"_{in}{}^2\epsilon}{4} + \frac{\pi(D"_{out}{}^2 - D"_{in}{}^2)}{4}\cdot\left(\frac{6v\cdot\eta}{h} + \gamma\left(\frac{\cos\vartheta_1+\cos\vartheta_2}{h}\right) + l\cdot\gamma\right)\right] \quad (5)$$

In this equation, D_{in}" and D_{out}" represent the inner and outer diameters of the contact surface under preload, r denotes the radius of the protuberance in contact with the substrate. The contact angles of the viscous liquid with the CNFs and the substrate are given by ϑ_1 and ϑ_2. Other parameters include atmospheric pressure (≈101.3 kPa), the viscosity-dependent volume change ratio (ϵ), sliding velocity (v), viscosity of the liquid (η), concentration-dependent surface tension (γ), and the number of adhesive structures (n).

Finally, the correlation between structural fidelity and functional performance was validated through normal adhesion tests of OIF patch tests on Silicon (Si) wafer substrate under identical viscosity conditions (Fig. 3(e) and Fig. S4 in the ESM). The experimental adhesion values were in close agreement with the theoretical predictions, showing a sharp increase as the imprinting pressure reached 500 MPa. OIF patch fabricated under imprinting pressures below 300 MPa exhibited adhesion forces lower than the preload pressure of 5 kPa, whereas those fabricated at 500 MPa achieved a robust normal adhesion force of approximately 8 kPa. These findings confirm that a pressure of 500 MPa is critical for ensuring both structural integrity and the functional adhesion performance of the OIF patch. Therefore, 500 MPa was determined to be the optimal imprinting pressure required to fabricate OIF patch.

3.4 Evaluation of Adhesion Stability and HA delivery performance on Dynamic Skin Interfaces

The practical applicability of the OIF patch as a transdermal delivery platform was evaluated by investigating its interfacial stability on authentic porcine skin, which serves as a clinically relevant model for human integument. As demonstrated in Fig. 4(a), the OIF patch achieved seamless adaptive adhesion with the porcine skin surface, whereas the conventional flat counterpart (Flat fibrous) exhibited significant void formation at the interface. To further challenge the adhesive robustness, adhesion performance was measured across various skin conditions, including dry, extremely dry, and cut surfaces exhibiting diverse stiffness (Fig. 4(b) and Fig. S5 in the ESM). Quantitative analysis of the normal and shear adhesion demonstrated that the OIF patch consistently outperformed the Flat fibrous across all skin conditions. Specifically, the OIF patch maintained a robust normal adhesion of approximately 5.3 kPa on extremely dry skin and approximately 5 kPa on cut skin, where the adhesion of Flat fibrous typically fails due to interfacial moisture or topographical disruptions (Fig. 4(c)). Furthermore, like the results observed in the

normal adhesion tests, the OIF patch demonstrated consistently higher shear resistance than the Flat fibrous and microneedle across all skin conditions (Fig. 4(d) and Fig. S6, S7 in the ESM). Notably, the performance gap between the two samples became more pronounced under the cut skin condition; while the shear adhesion of the Flat fibrous sharply declined to approximately 3 kPa, the OIF patch preserved a robust adhesion approximately 5.2 kPa. These results indicate that the hierarchical architecture of the OISC facilitates adaptive adhesion and maximizes the interfacial contact area, providing reliable adhesion stability even on extremely dry and damaged skin. The adhesion performance of the OIF patch under dynamic movement was further investigated using a custom-built bending apparatus (Fig. 4(e-i)). After attaching the porcine skin on a custom-built bending apparatus, the adhesion performance of OIF patch and Flat fibrous on the porcine skin in the bending state was measured by bending it at an angle (Fig. S8 in the ESM). The Flat fibrous experienced rapid delamination and the enlargement of interfacial voids as the bending angle increased, leading to a complete loss of contact. In stark contrast, the OIF patch maintained intimate and adaptive skin adhesion without any observable detachment, even under severe bending states (Fig. 4(e-ii)). Furthermore, the long-term reliability of this adhesion was confirmed through a cyclic bending test, where the OIF patch preserved its adaptive adhesion with porcine skin interface without structural damage or peeling even after 100 cycles of repeated deformation (Fig. 4(e-iii)). To verify the biocompatibility and user-friendliness of the platform, FT-IR spectra of the skin surface were analyzed after the removal and rinsing of the patch. The results confirmed that the skin surface was identical to the control group, indicating that the OIF patch leaves no chemical residue, thereby ensuring a safe and fully non-invasive application process (Fig. 4(f)). Additionally, the OIF patch did not induce observable skin barrier disruption or visible skin damage (Fig. S9). The ultimate functional benefit of the adaptive interfacial adhesion was validated through the transdermal delivery of rhodamine B-tagged HA (Fig.4(g) and Fig. S10 in the ESM). Confocal microscopy analysis revealed that the delivery depth was significantly enhanced by the OIF patch compared to the Flat fibrous. Under a flat skin state, the OIF patch demonstrated a progressively increasing delivery depth over 30 minutes, significantly exceeding the performance of the Flat fibrous. The advantage of the OIF patch was even more pronounced under bending-state skin conditions. While the delivery depth of the Flat fibrous was severely compromised due to patch detachment and the resulting interruption of the diffusion path, the OIF patch maintained consistent and deep penetration of the fluorescent particles. Quantitative comparison in Fig. 4(h) highlights that at an application time of 30 minutes, the OIF patch achieved a delivery depth of approximately 140 μm on bending skin, which is nearly 3.5 times greater than the depth achieved by the Flat fibrous (≈40 μm). These findings indicate that the OIF patch not only ensures adaptive skin adhesion but also promotes active ingredient delivery by eliminating voids and maintaining close contact during dynamic skin deformation. Consequently, the OIF patch represents a highly effective and versatile platform for advanced transdermal therapy in practical, dynamic environments.

3.5 Clinical Efficacy of OIF patch

HA is a key ingredient used to improve skin due to its hydrating and anti-aging properties [48]. To assess the clinical efficacy of OIF patch in enhancing skin quality, several dermatological parameters, specifically roughness, pores, and fine lines were monitored over a 14-day application period. As illustrated in Fig. 5(a), the study compared two delivery methods: topical HA application and the OIF patch system. Treatments were administered daily for 20 minutes to the back of the hand in a flexed state. To minimize environmental bias, all participants were maintained under constant ambient temperature and humidity. Participants were selected based on specific age and gender criteria, and 2D skin images and quantitative data were recorded before and after application (Fig. S11 in the ESM). The analysis of skin roughness utilized topographic mapping, where depressions were indicated in red/yellow and protrusions in blue/purple (Fig. 5(b) and Fig. S11 in the ESM). After 14 days, the OIF patch group demonstrated a significant improvement in average roughness, achieving a reduction of ≈44%, which substantially outperformed the ≈19% observed in the topical group (Fig. 5(c), Fig. S12, and S13 in the ESM). Additionally, the maximum height difference in the roughness profile improved by ≈51% with OIF patch, compared to ≈34% for the topical application (Fig. 5(d) and Fig. S13 in the ESM). Pore analysis, highlighted in light green (Fig. 5(e) and Fig. S11 in the ESM), also showed marked enhancements. The OIF patch group exhibited a ≈80% decrease in pore counts, while the topical group showed a ≈47% reduction (Fig. 5(f) and Fig. S14 in the ESM). Furthermore, the CNFs-OISC treatment resulted in the greatest improvements in mean pore area (≈81%) and depth (≈51%), whereas the topical group achieved improvements of ≈53% and ≈23%, respectively (Fig. 5(g), 5(h), and Fig. S14 in the ESM). Finally, the treatment effectively diminished fine lines (defined as wrinkles < 0.7 mm), as shown in Fig. 5(i) and Fig. S11 in the ESM. The most pronounced reduction in fine line counts was observed in the OIF patch group (≈91%), compared to ≈50% in the topical group (Fig. 5(j) and Fig. S15 in the ESM). The OIF patch group also showed significant improvements in fine line length (≈94%), depth (≈63%), and width (≈48%). In contrast, the topical application group recorded improvements of ≈38% in length, ≈30% in depth, and ≈11% in width (Fig. 5(k), 5(l), Fig. S12 and S15 in the ESM). These findings collectively demonstrate the superior clinical performance of the OIF patch delivery system over conventional topical methods.

4 Conclusions

In this study, we developed a bioinspired cellulose nanofiber-based transdermal patch (OIF patch) that integrates OISC to overcome the limitations of conventional patches under dynamic skin deformations. Utilizing a straightforward and scalable thermal imprinting process, we identified 150 °C and 500 MPa as the optimal fabrication conditions to ensure structural integrity and resistance to collapse in high-viscosity environments. The adhesion mechanism of OIF patch, driven by structural deformation-induced localized

negative pressure, ensures robust and adaptive adhesion. This interfacial stability allows the patch to maintain robust adhesion across diverse skin conditions, and through severe bending deformations of up to 90°. Consequently, OIF patch enabled stable and continuous HA delivery, achieving a 3.5-fold enhancement in transdermal delivery depth compared to Flat fibrous under dynamic bending conditions. The clinical viability of the platform under bending conditions was further confirmed through a 14-day study, where OIF patch with HA demonstrated superior efficacy in improving key skin parameters-including roughness, pores, and fine lines-compared to Flat fibrous. Given its biocompatibility, ease of manufacturing, and reliable performance on deformed skin, the OIF patch platform holds significant potential as a versatile and user-friendly system for advanced, non-invasive transdermal therapies. However, as this investigation serves as a pilot feasibility study, further research is necessary as the rate of skin condition improvement may be influenced by structural and morphological variations of the skin determined by intrinsic factors such as race, age, and gender. Additionally, future advancements in mold material design and CNF reactivity offer the potential to enhance industrial scalability by reducing the processing energy and equipment costs required for large-scale production. Furthermore, personalized skin improvement effects can be expected by incorporating various bioactive ingredients with potent skin enhancing properties into the OIF patch system.

Electronic Supplementary Material: Supplementary material is available in the online version of this article at https://doi.org/10.26599/NR.2026.94908813.

Data availability

All data needed to support the conclusions in the paper are presented in the manuscript and/or the Electronic Supplementary Material. Additional data related to this paper may be requested from the corresponding author upon request.

Acknowledgements

The authors gratefully acknowledge the support from the National Research Foundation of Korea (RS-2024-00352352) and by the Korean Fund for Regenerative Medicine (KFRM) grant funded by the Korea government (the Ministry of Science and ICT, the Ministry of Health & Welfare). (No. 25A0102L1). This study was conducted in part with the support of the industry-academia cooperation research of Mimetics Co., Ltd.

Declaration of competing interest

All the contributing author(s) report(s) no conflict of interests in this work.”

Author contribution statement

Minjin Kim: Data curation, Formal analysis, Investigation, Methodology, Writing – original draft. Minwoo Song: Conceptualization, Formal analysis, Methodology, Writing – original draft. Hyoung-Ki Park: Funding acquisition, Resources, Writing – original draft. Gui Won Hwang: Software. Jihun Son: Methodology. Changrok Park: Investigation. Gyun Ro Kang: Investigation. Changhyun Pang: Funding acquisition, Supervision, Writing – review & editing

Informed consent

Not applicable

Ethics statement

Not applicable

Use of AI statement

None.

References

[1] Prausnitz, M. R.; Langer, R. Transdermal drug delivery. *Nature biotechnology* **2008**, *26*, 1261-1268.

[2] Jung, H.;Kim, M. K.;Lee, J. Y.;Choi, S. W.; Kim, J. Adhesive hydrogel patch with enhanced strength and adhesiveness to skin for transdermal drug delivery. *Advanced Functional Materials* **2020**, *30*, 2004407.

[3] Jiang, T.;Xu, G.;Chen, G.;Zheng, Y.;He, B.; Gu, Z. Progress in transdermal drug delivery systems for cancer therapy. *Nano Research* **2020**, *13*, 1810-1824.

[4] Prausnitz, M. R.;Mitragotri, S.; Langer, R. Current status and future potential of transdermal drug delivery. *Nature reviews Drug discovery* **2004**, *3*, 115-124.

[5] Kim, M.;Song, M.;Son, J.;Hwang, G. W.;Park, H. K.; Pang, C. Effective HA-Loading Strategy in Internal Dome-Assisted Suction Cups for Enhanced Transdermal Delivery Under Vertical Adhesion and Vibration. *Advanced Functional Materials* **2025**, e19672.

[6] Zhu, Z.;Wang, J.;Pei, X.;Chen, J.;Wei, X.;Liu, Y.;Xia, P.;Wan, Q.;Gu, Z.; He, Y. Blue-ringed octopus-inspired microneedle patch for robust tissue surface adhesion and active injection drug delivery. *Science advances* **2023**, *9*, eadh2213.

[7] Lim, D.;Song, M.;Kim, M.;Park, H.-K.;Kim, D. W.; Pang, C. Bioinspired suction-driven strategies with nanoscale skin-controllable adhesive architectures for efficient liquid formulated transdermal patches. *ACS nano* **2025**, *19*, 13567-13590.

[8] Zhou, Y.;Jia, X.;Pang, D.;Jiang, S.;Zhu, M.;Lu, G.;Tian, Y.;Wang, C.;Chao, D.; Wallace, G. An integrated Mg battery-powered iontophoresis patch for efficient and controllable transdermal drug delivery. *Nature Communications* **2023**, *14*, 297.

[9] Han, X.;Wang, F.;Shen, J.;Chen, S.;Xiao, P.;Zhu, Y.;Yi, W.;Zhao, Z.;Cai, Z.; Cui, W. Ultrasound Nanobubble Coupling Agent for Effective Noninvasive Deep-Layer Drug Delivery. *Advanced Materials* **2024**, *36*, 2306993.

[10] Xu, X.;Guo, L.;Liu, H.;Zhou, Z.;Li, S.;Gu, Q.;Ding, S.;Guo, H.;Yan, Y.; Lan, Y. Stretchable electronic facial masks for skin electroporation. *Advanced Functional Materials* **2024**, *34*, 2311144.

[11] Liu, L.;Yin, Z.;Lu, X.;Wang, H.;Ye, J.;Zhang, Y.;Zhou, C.;Shi, J.;Luo, J.; Wang, X. Light-converting microneedle patch for cutaneous UV phototherapy in psoriasis with enhanced safety and efficiency. *Nano Research* **2024**, *18*.

[12] Sun, W.;Jiang, H.;Wu, X.;Xu, Z.;Yao, C.;Wang, J.;Qin, M.;Jiang, Q.;Wang, W.; Shi, D. Strong dual-crosslinked hydrogels for ultrasound-triggered drug delivery. *Nano Research* **2019**, *12*, 115-119.

[13] Rasouli, R.;Barhoum, A.;Bechelany, M.; Dufresne, A. Nanofibers for biomedical and healthcare applications. *Macromolecular bioscience* **2019**, *19*, 1800256.

[14] Fu, L.;Feng, Q.;Chen, Y.;Fu, J.;Zhou, X.; He, C. Nanofibers for the immunoregulation in biomedical applications. *Advanced Fiber Materials* **2022**, *4*, 1334-1356.

[15] Song, M.;Park, H.-K.;Kim, M.;Hwang, G. W.;Son, J.;Kang, G. R.;Lee, J.; Pang, C. Skin-adaptive nanofiber-based adhesive electronics with octopus-like 3D suction cups for enhanced transdermal delivery. *npj Flexible Electronics* **2025**, *9*, 54.

[16] Bi, P.;Zhang, M.;Li, S.;Lu, H.;Wang, H.;Liang, X.;Liang, H.; Zhang, Y. Ultra-sensitive and wide applicable strain sensor enabled by carbon nanofibers with dual alignment for human machine interfaces. *Nano Research* **2023**, *16*, 4093-4099.

[17] Kamble, P.;Sadarani, B.;Majumdar, A.; Bhullar, S. Nanofiber based drug delivery systems for skin: A promising therapeutic approach. *Journal of Drug Delivery Science and Technology* **2017**, *41*, 124-133.

[18] Hu, X.;Liu, S.;Zhou, G.;Huang, Y.;Xie, Z.; Jing, X. Electrospinning of polymeric nanofibers for drug delivery applications. *Journal of controlled release* **2014**, *185*, 12-21.

[19] Ogueri, K. S.; Laurencin, C. T. Nanofiber technology for regenerative engineering. *ACS nano* **2020**, *14*, 9347-9363.

[20] Kajdič, S.;Planinšek, O.;Gašperlin, M.; Kocbek, P. Electrospun nanofibers for customized drug-delivery systems. *Journal of Drug Delivery Science and Technology* **2019**, *51*, 672-681.

[21] Wildy, M.; Lu, P. Electrospun nanofibers: shaping the future of controlled and responsive drug delivery. *Materials* **2023**, *16*, 7062.

[22] Ki, C. S.;Baek, D. H.;Gang, K. D.;Lee, K. H.;Um, I. C.; Park, Y. H. Characterization of gelatin nanofiber prepared from gelatin–formic acid solution. *Polymer* **2005**, *46*, 5094-5102.

[23] Kim, S. H.;Nam, Y. S.;Lee, T. S.; Park, W. H. Silk fibroin nanofiber. Electrospinning, properties, and structure. *Polymer Journal* **2003**, *35*, 185-190.

[24] El-Aassar, M.;Ibrahim, O. M.; Al-Oanzi, Z. H. Biotechnological applications of polymeric nanofiber platforms loaded with diverse bioactive materials. *Polymers* **2021**, *13*, 3734.

[25] Xue, J.;Wu, T.;Dai, Y.; Xia, Y. Electrospinning and electrospun nanofibers: methods, materials, and applications. *Chemical reviews* **2019**, *119*, 5298-5415.

[26] El-Seedi, H. R.;Said, N. S.;Yosri, N.;Hawash, H. B.;El-Sherif, D. M.;Abouzid, M.;Abdel-Daim, M. M.;Yaseen, M.;Omar, H.; Shou, Q. Gelatin nanofibers: Recent insights in synthesis, bio-medical applications and limitations. *Heliyon* **2023**, *9*.

[27] Li, T.;Sun, M.; Wu, S. State-of-the-art review of electrospun gelatin-based nanofiber dressings for wound healing applications. *Nanomaterials* **2022**, *12*, 784.

[28] Min, B.-M.;Lee, G.;Kim, S. H.;Nam, Y. S.;Lee, T. S.; Park, W. H. Electrospinning of silk fibroin nanofibers and its effect on the adhesion and spreading of normal human keratinocytes and fibroblasts in vitro. *Biomaterials* **2004**, *25*, 1289-1297.

[29] Hu, X.;Shmelev, K.;Sun, L.;Gil, E.-S.;Park, S.-H.;Cebe, P.; Kaplan, D. L. Regulation of silk material structure by temperature-controlled water vapor annealing. *Biomacromolecules* **2011**, *12*, 1686-1696.

[30] Johari, N.;Moroni, L.; Samadikuchaksaraei, A. Tuning the conformation and mechanical properties of silk fibroin hydrogels. *European Polymer Journal* **2020**, *134*, 109842.

[31] Farokhi, M.;Mottaghitalab, F.;Reis, R. L.;Ramakrishna, S.; Kundu, S. C. Functionalized silk fibroin nanofibers as drug carriers: Advantages and challenges. *Journal of Controlled Release* **2020**, *321*, 324-347.

[32] Promsuk, J.;Manissorn, J.;Laomeephol, C.;Luckanagul, J. A.;Methachittipan, A.;Tonsomboon, K.;Jenjob, R.;Yang, S.-G.;Thongnuek, P.; Wangkanont, K. Optimizing protein delivery rate from silk fibroin hydrogel using silk fibroin-mimetic peptides conjugation. *Scientific Reports* **2024**, *14*, 4428.

[33] Liu, Z.;Zhang, S.;He, B.;Wang, S.; Kong, F. Synthesis of cellulose aerogels as promising carriers for drug delivery: a review. *Cellulose* **2021**, *28*, 2697-2714.

[34] El Allaoui, B.;Benzeid, H.;Zari, N.;el kacem Qaiss, A.; Bouhfid, R. Functional cellulose-based beads for drug delivery: Preparation, functionalization, and applications. *Journal of Drug Delivery Science and Technology* **2023**, *88*, 104899.

[35] Janmohammadi, M.;Nazemi, Z.;Salehi, A. O. M.;Seyfoori, A.;John, J. V.;Nourbakhsh, M. S.; Akbari, M. Cellulose-based composite scaffolds for bone tissue engineering and localized drug delivery. *Bioactive Materials* **2023**, *20*, 137-163.

[36] Chen, N.;Wang, H.;Ling, C.;Vermerris, W.;Wang, B.; Tong, Z. Cellulose-based injectable hydrogel composite for pH-responsive and controllable drug delivery. *Carbohydrate polymers* **2019**, *225*, 115207.

[37] Ai, Y.;Lin, Z.;Zhao, W.;Cui, M.;Qi, W.;Huang, R.; Su, R. Nanocellulose-based hydrogels for drug delivery. *Journal of Materials Chemistry B* **2023**, *11*, 7004-7023.

[38] Huo, Y.;Liu, Y.;Xia, M.;Du, H.;Lin, Z.;Li, B.; Liu, H. Nanocellulose-based composite materials used in drug delivery systems. *Polymers* **2022**, *14*, 2648.

[39] Kolakovic, R.;Peltonen, L.;Laukkanen, A.;Hirvonen, J.; Laaksonen, T. Nanofibrillar cellulose films for controlled drug delivery. *European Journal of Pharmaceutics and Biopharmaceutics* **2012**, *82*, 308-315.

[40] Won, T.;Goh, M.;Lim, C.;Moon, J.;Lee, K.;Park, J.;Chung, K.;Kim, Y.;Lee, S.; Hong, H. J. Recent progress in cellulose nanofibril hydrogels for biomedical applications. *Polymers* **2025**, *17*, 2272.

[41] Wang, T.;Shi, X.;Wang, Y.;Sun, H.;Sun, Y.;Wang, G.; Jiang, H. Lidocaine-loaded iontophoresis-driven fiber-based microneedle patch for controllable and long-lasting transdermal local analgesia. *Advanced Fiber Materials* **2025**, *7*, 281-295.

[42] Wai Cheung, T.;Yang, C.; Li, L. An integrated design of self-care textile wearables: exploration of thermal-stimuli effects and drug delivery function. *Textile Research Journal* **2019**, *89*, 2553-2568.

[43] Daelemans, L.;Van Paepegem, W.;D'hooge, D. R.; De Clerck, K. Excellent nanofiber adhesion for hybrid polymer materials with high toughness based on matrix interdiffusion during chemical conversion. *Advanced Functional Materials* **2019**, *29*, 1807434.

[44] Morad, H.;Jahanshahi, M.;Akbari, J.;Saeedi, M.;Gill, P.; Enayatifard, R. Novel topical and transdermal delivery of colchicine with chitosan based biocomposite nanofiberous system; formulation, optimization, characterization, ex vivo skin deposition/permeation, and anti-melanoma evaluation. *Materials Chemistry and Physics* **2021**, *263*, 124381.

[45] Talebi, N.;Lopes, D.;Lopes, J.;Macário-Soares, A.;Dan, A. K.;Ghanbari, R.;Kahkesh, K. H.;Peixoto, D.;Giram, P. S.; Raza, F. Natural polymeric nanofibers in transdermal drug delivery. *Applied Materials Today* **2023**, *30*, 101726.

[46] Dzenis, Y. Spinning continuous fibers for nanotechnology. *Science* **2004**, *304*, 1917-1919.

[47] Li, X.;Cho, B.;Martin, R.;Seu, M.;Zhang, C.;Zhou, Z.;Choi, J. S.;Jiang, X.;Chen, L.; Walia, G. Nanofiber-hydrogel composite–mediated angiogenesis for soft tissue reconstruction. *Science translational medicine* **2019**, *11*, eaau6210.

[48] Bravo, B.;Correia, P.;Goncalves Junior, J. E.;Sant'Anna, B.; Kerob, D. Benefits of topical hyaluronic acid for skin quality and signs of skin aging: From literature review to clinical evidence. *Dermatologic therapy* **2022**, *35*, e15903.

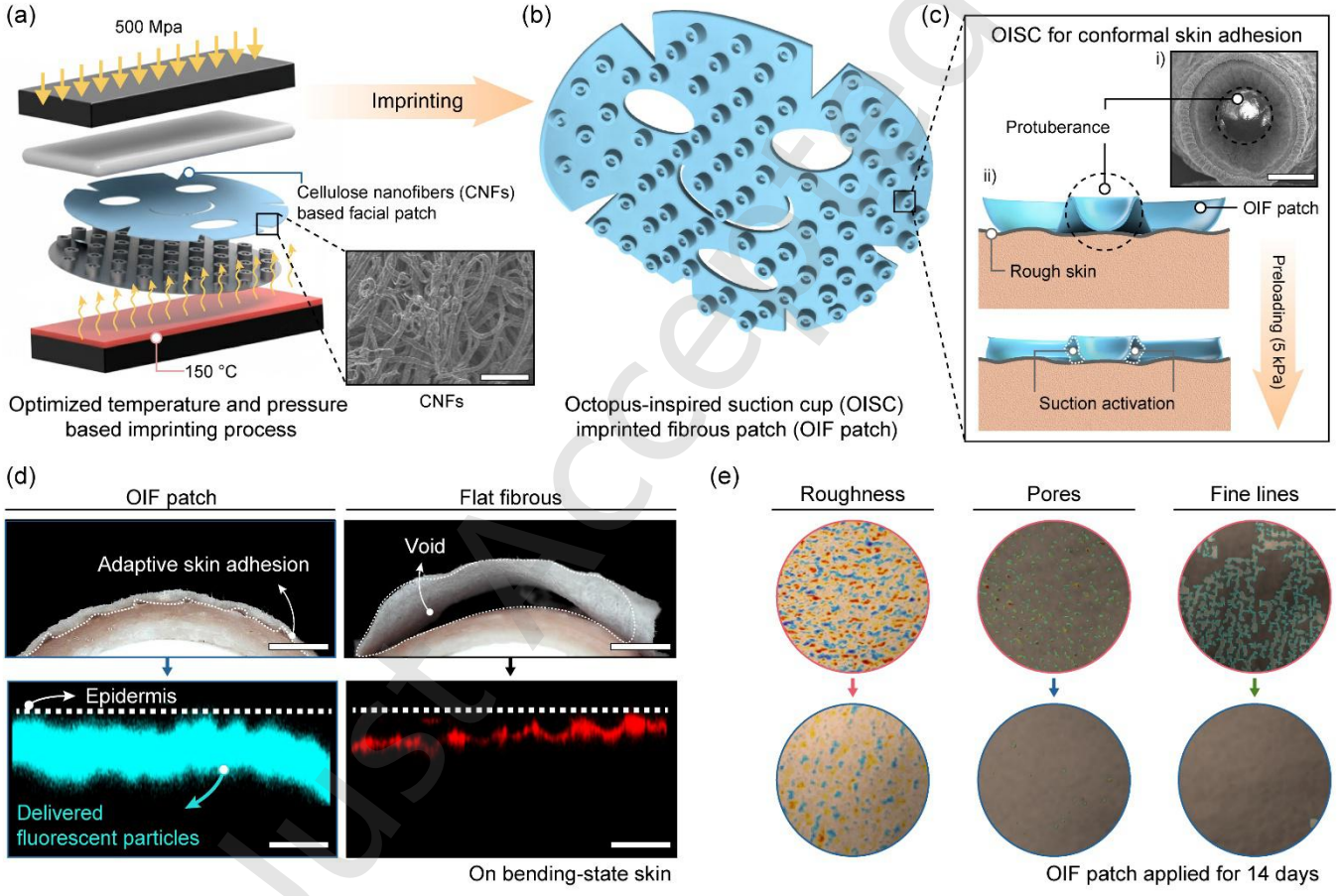

Figure 1 (a) Schematic of the fabrication process for OIF patch (Octopus-inspired suction cup (OISC) imprinted fibrous patch). Inset shows low-magnification SEM images of CNFs (scale: 100 μm). (b) Schematic of OIF patch. (c) OISC for conformal skin adhesion. i) Low magnification scanning electron microscope (SEM) image of sucker of an octopus (scale: 1 mm). ii) Schematic of the adhesion mechanism in OISC. The mechanism involves OISC providing adaptive adhesion with the rough skin through suction activation within the structure. (d) Adhesion performance of OIF patch and Flat fibrous on porcine skin (top). Confocal microscopy analysis fluorescent particles diffusion through porcine skin under bending state after 20 min of application (bottom). (e) Representative images of skin conditions (roughness, pores, and fine lines) before (top) and after (bottom) OIF patch application.

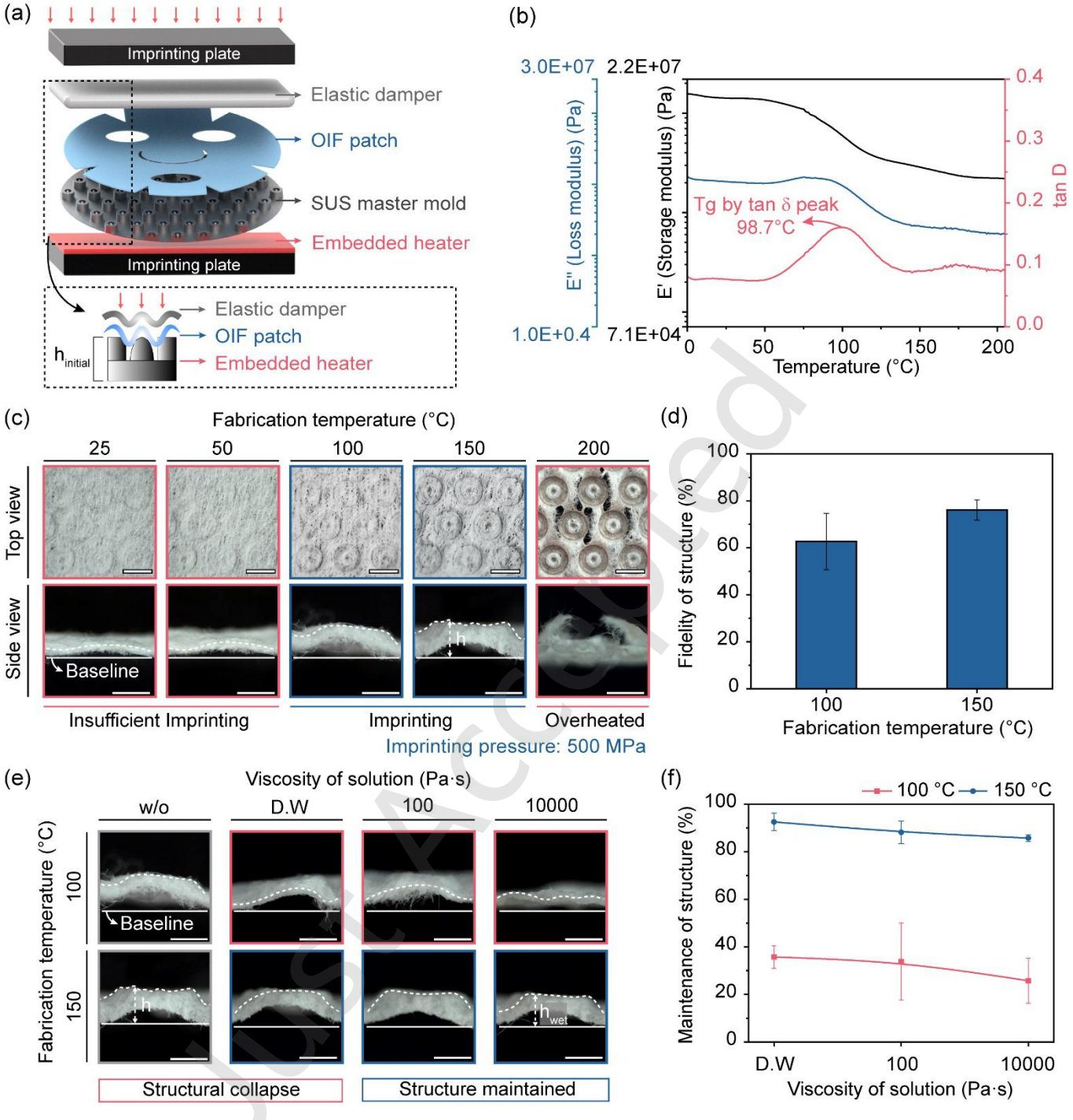

Figure 2 (a) Schematic of the fabrication process for the OIF patch. (b) Dynamic mechanical analysis (DMA) of the CNFs to determine the glass transition temperature (Tg). (c) Representative top-view (top) and side-view (bottom) images of OIF patch fabricated at various temperatures (25, 50, 100, 150, and 200 °C) under an imprinting pressure of 500 MPa (scale: top, 1 mm; bottom, 0.6mm). (d) Quantitative analysis of the structural fidelity (%) of OIF patch at different fabrication temperatures (100 and 150 °C); n = 10. (e) Photographs of OIF patch fabricated at 100 and 150 °C following the addition of solutions with different viscosities (without liquid, deionized water (D.W), 100, and 10000 Pa·s). (f) Structural maintenance (%) of OIF patch fabricated at 100 and 150 °C following the addition of solutions with different viscosities (D.W water, 100, and 10000 Pa·s); *n* = 10.

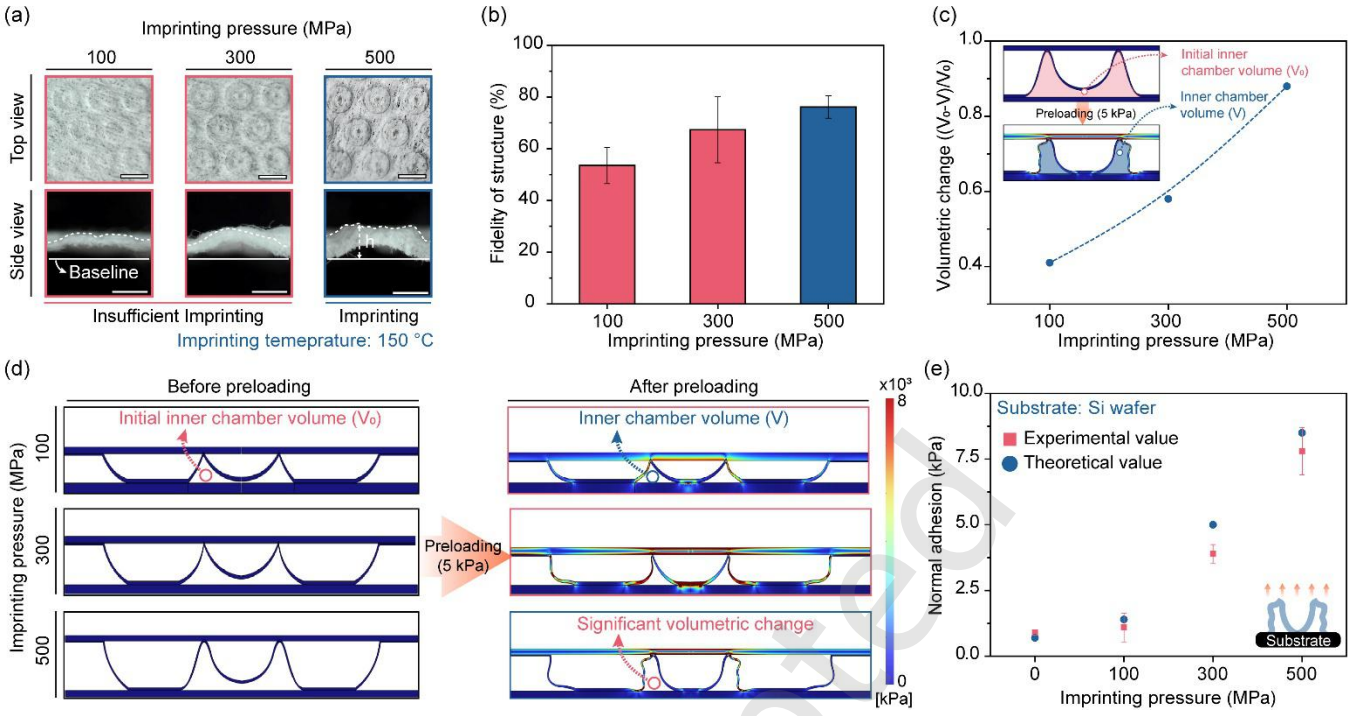

Figure 3 (a) Representative top-view (top) and side-view (bottom) images of OIF patch fabricated at various pressures (100, 300, and 500 MPa) under an imprinting temperature of 150 °C (scale: top, 1 mm; bottom, 0.6mm). (b) Quantitative analysis of the structural fidelity (%) of OIF patch at different imprinting pressures (100, 300, and 500 MPa); n = 10. (c) Volumetric change rate in the inner chamber of OIF patch fabricated at various imprinting pressures (100, 300, and 500 MPa) under a 5 kPa preload. (d) Finite element method (FEM) simulations comparing OIF patch fabricated at various imprinting pressures (100, 300, and 500 MPa) under a preload of 5 kPa. (e) Normal adhesion performance on a Si wafer substrate of OIF patch fabricated at different imprinting pressures (0, 100, 300, and 500 MPa), comparing theoretical (blue dots) and experimental values (red dots); n = 10.

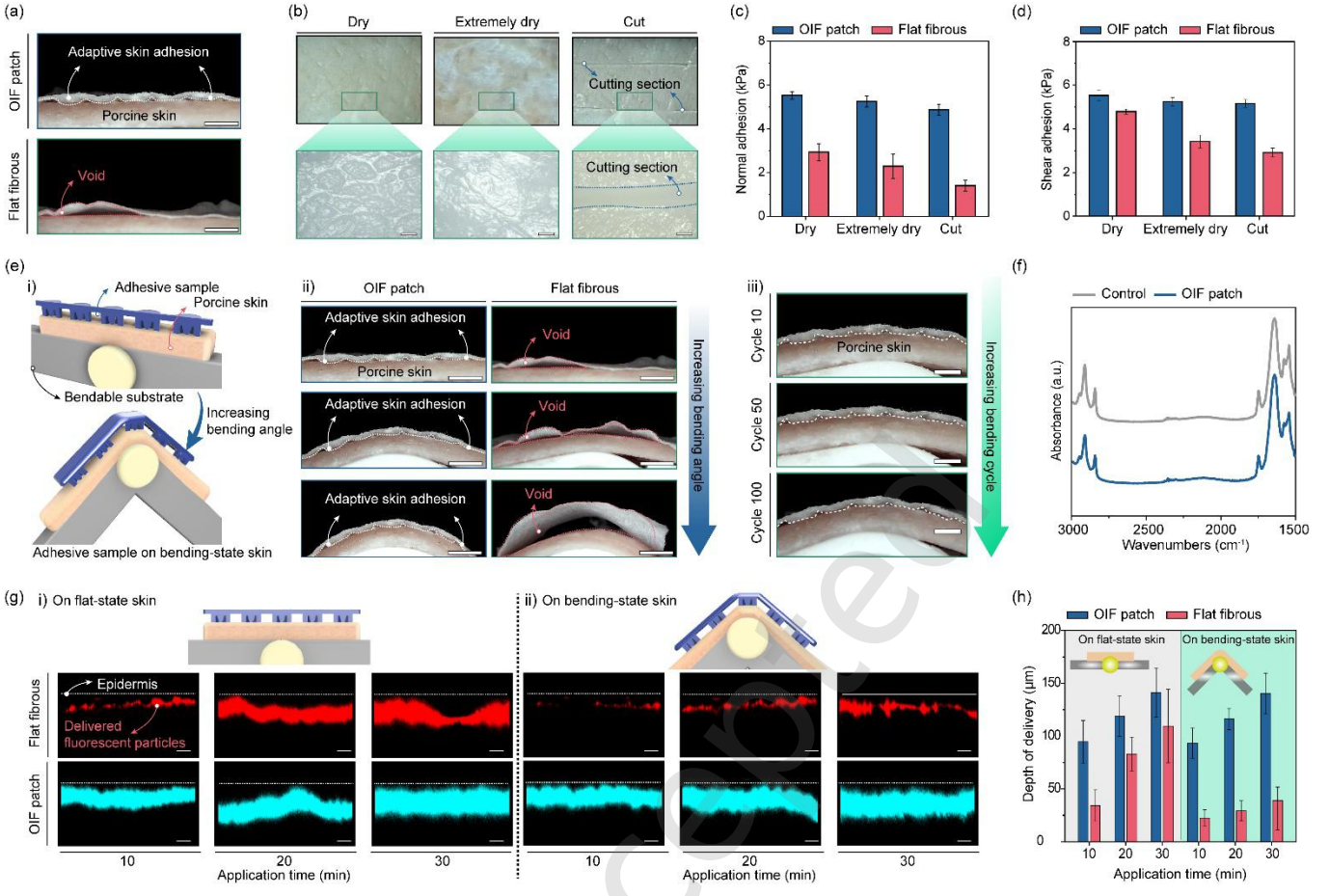

Figure 4 (a) Adhesion performance of OIF patch and Flat fibrous on authentic porcine skin. (b) Photographs (top) and optical microscopy (OM) images (bottom) of porcine skin in dry, extremely dry, and cut conditions (scale: 100 μm). (c) Normal adhesion performance of OIF patch and Flat fibrous on various skin conditions; n = 10. (d) Shear adhesion performance of OIF patch and Flat fibrous on various skin conditions; n = 10. (e) i) Schematic of experimental setup using custom-built equipment to measure the adhesion performance of adhesives on bending-state porcine skin. ii) Adhesion performance of OIF patch and Flat fibrous on authentic porcine skin under varying degrees of bending, using custom-built equipment. iii) Adhesion performance of OIF patch as a function of repeated bending cycles. (f) FT-IR spectra of surface residues after application and rinsing of OIF patch from porcine skin. (g) Confocal microscopy analysis of rhodamine B-tagged HA diffusion through porcine skin in (i) flat and (ii) bending states at various application times (10, 20, and 30 min). (h) Comparison of the delivery depth of fluorescent particles into porcine skin on both flat-state and bending-state skin at various application times (blue columns: OIF patch, red columns: Flat fibrous); n = 10.

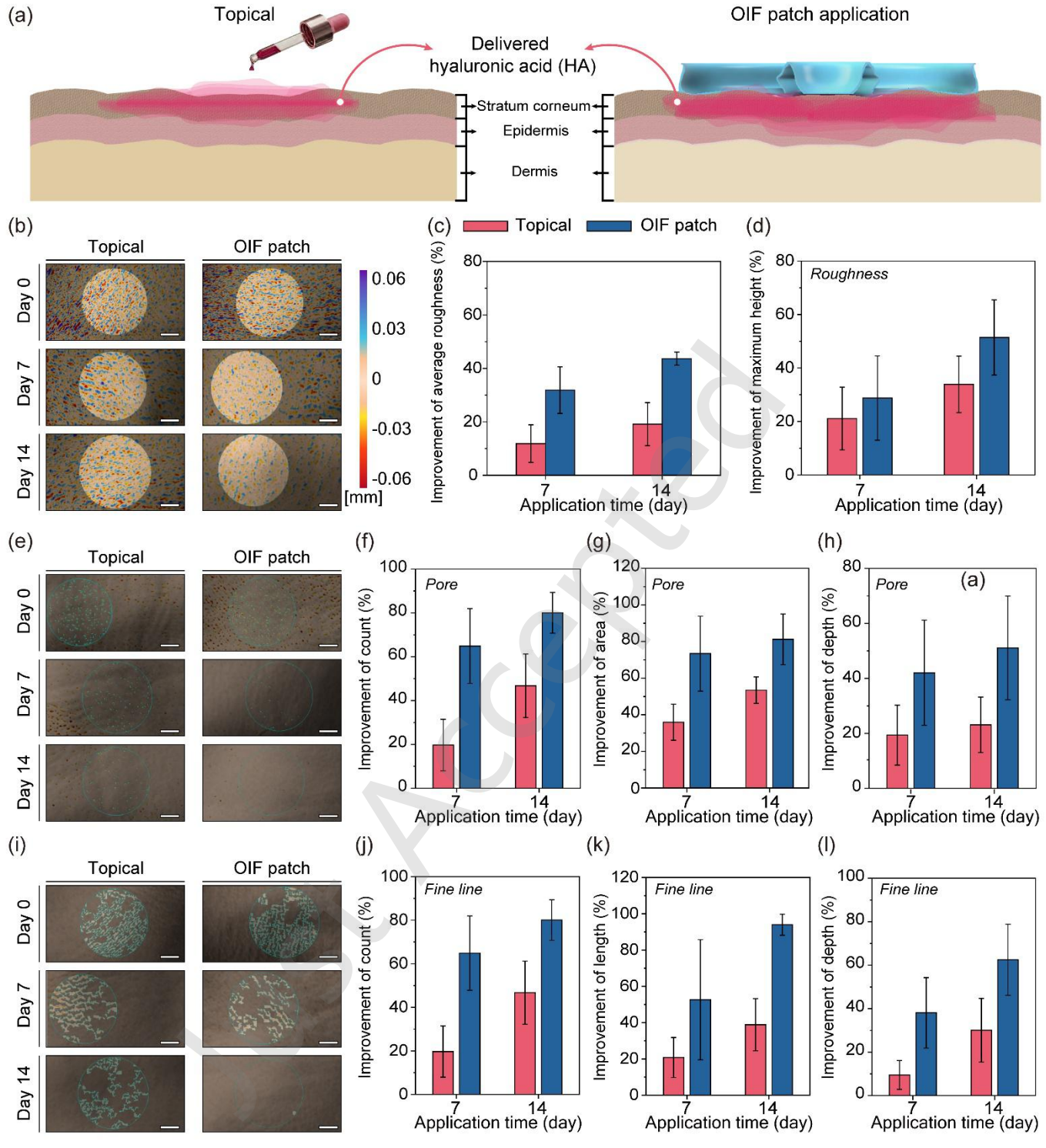

Figure 5 (a) Schematic of various HA delivery methods to the skin (topical application and OIF patch). (b–d) Skin roughness analysis across two application methods (red: topical, blue: OIF patch). (b) Representative skin roughness images (scale: 1 mm). (c) Degree of improvement in the average deviation from a straight line. (d) Degree of improvement in the height difference between the peak and the valley; n = 16. (e–h) Pore analysis across two application methods. (e) Representative pore images (scale: 1 mm). (f) Degree of improvement in the pore count. (g) Degree of improvement in the mean pore area. (h) Degree of improvement in the average pore depth; n = 16. (i–l) Fine line analysis across two application methods. (i) Representative fine line images (scale: 1 mm). (j) Degree of improvement in the number of fine lines. (k) Degree of improvement in the total fine line length. (l) Degree of improvement in the average fine line depth; n = 16.

Electronic Supplementary Material

Minjin Kim[1, §], Minwoo Song[1, §], Hyoung-Ki Park[1,2 §], Gui Won Hwang[1], Jihun Son[1], Changrok Park[1], Gyun Ro Kang[1], and Changhyun Pang[1,3] ✉

[1] *School of Chemical Engineering Sungkyunkwan University (SKKU), 2066 Seobu-ro, Jangan-gu, Suwon 16419, Republic of Korea*

[2] *Mimetics Co., Ltd, 2066 Seobu-ro, Jangan-gu, Suwon 16419, Republic of Korea*

[3] *Samsung Advanced Institute for Health Science & Technology (SAIHST) Sungkyunkwan University (SKKU), Seoul, 06351, Republic of Korea*

[§] *Minjin Kim, Minwoo Song, and Hyoung-Ki Park contributed equally to this work.*

Supporting information to https://doi.org/10.26599/NR.2026.94908813

Address correspondence to chpang@skku.edu

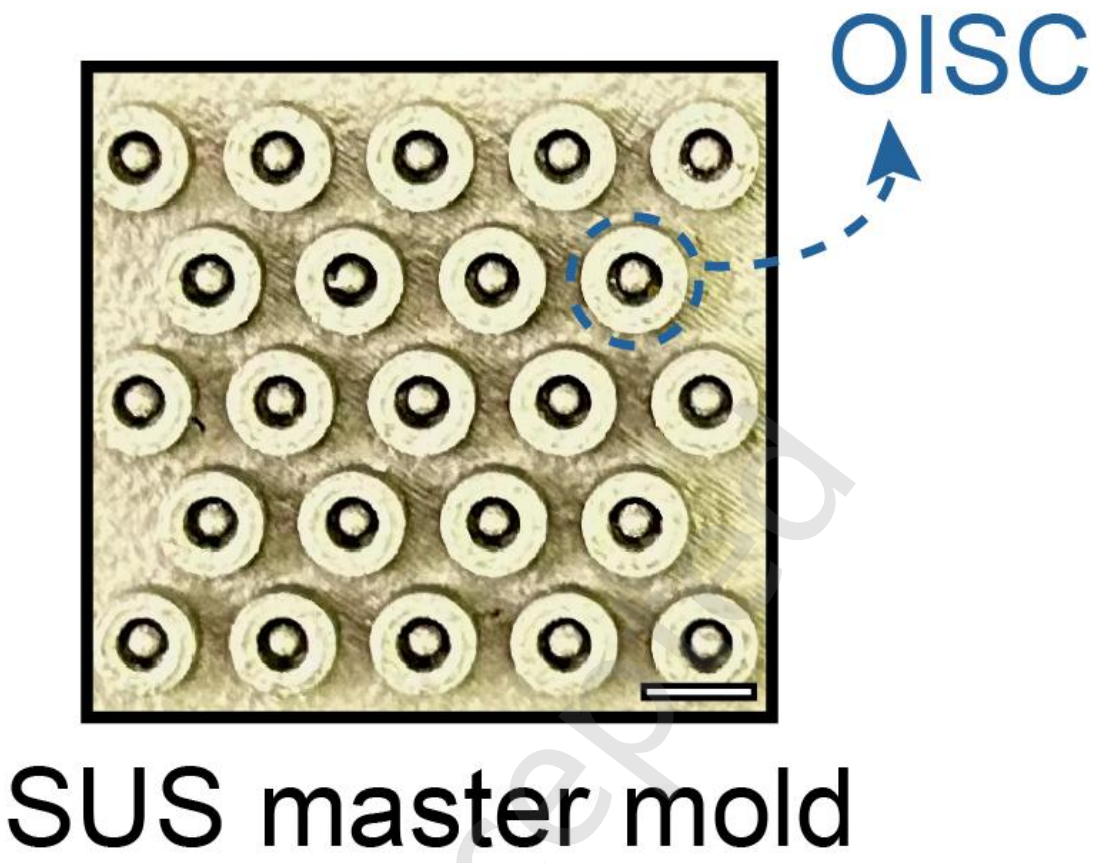

Figure S1 Image of SUS master mold (scale: 3mm).

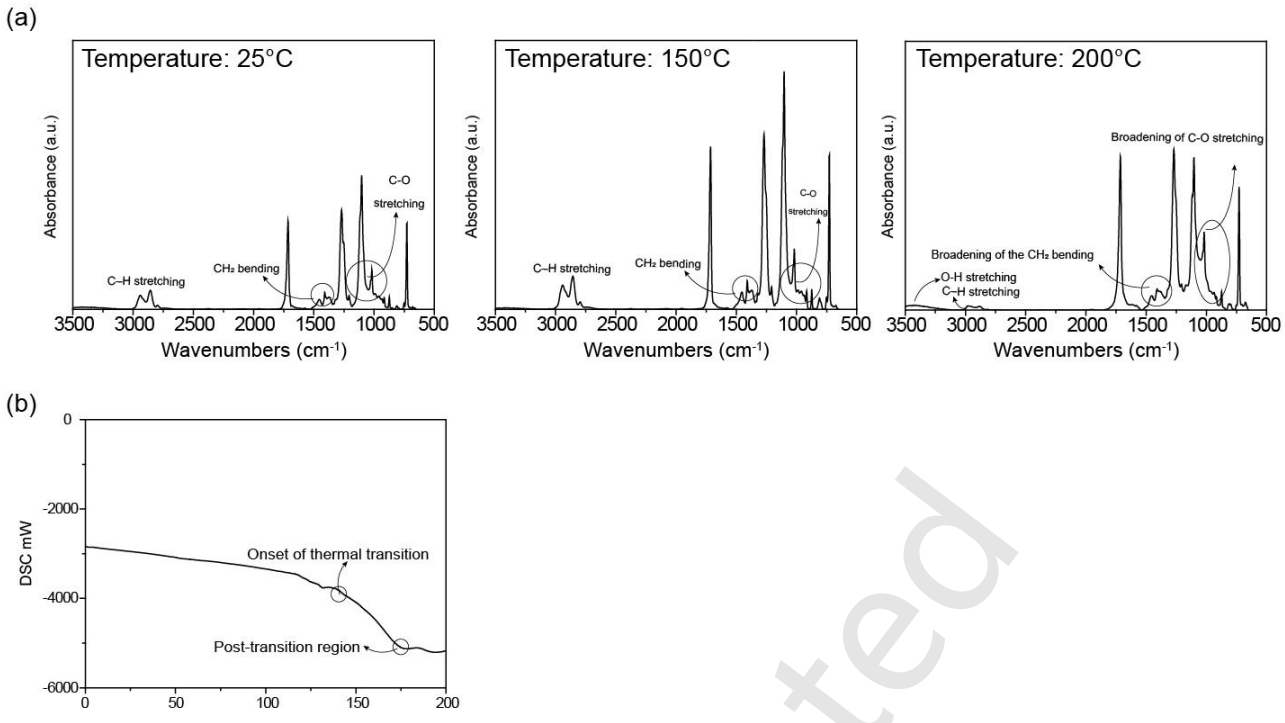

Figure S2 (a) Temperature-dependent FT-IR spectra of CNFs (25, 150, and 200 °C). (b) DSC thermogram of CNFs under thermal loading.

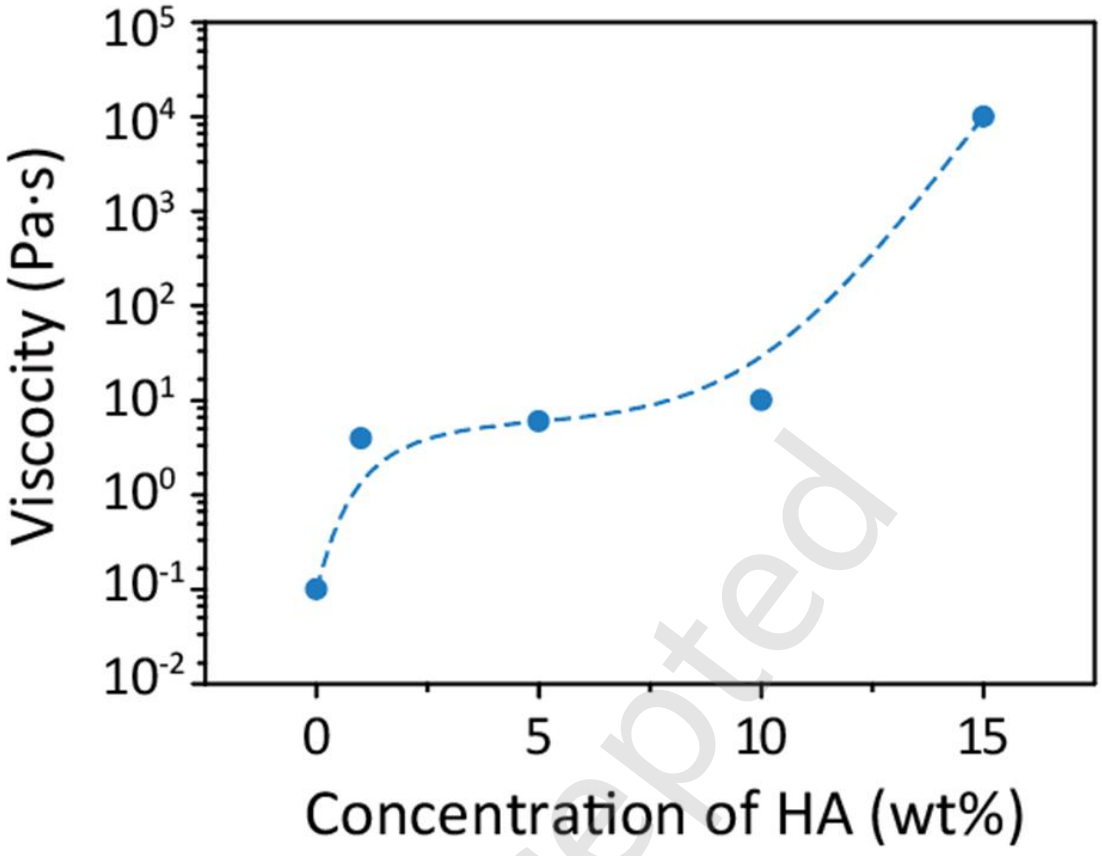

Figure S3 Viscosity of HA solutions according to change in HA concentration.

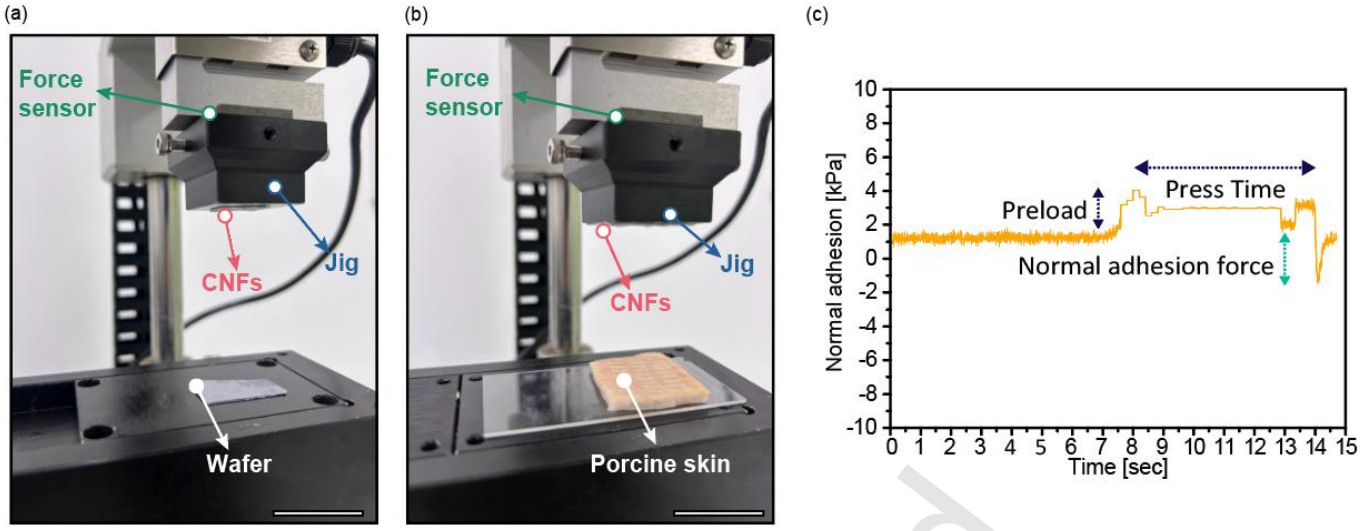

Figure S4 Setup for adhesion tests. Measurement of normal adhesion performance of the CNFs on (a) Si wafer and (b) porcine skin surface using custom-built equipment (scale: 1 cm). (c) Representative time-dependent profile of normal adhesion.

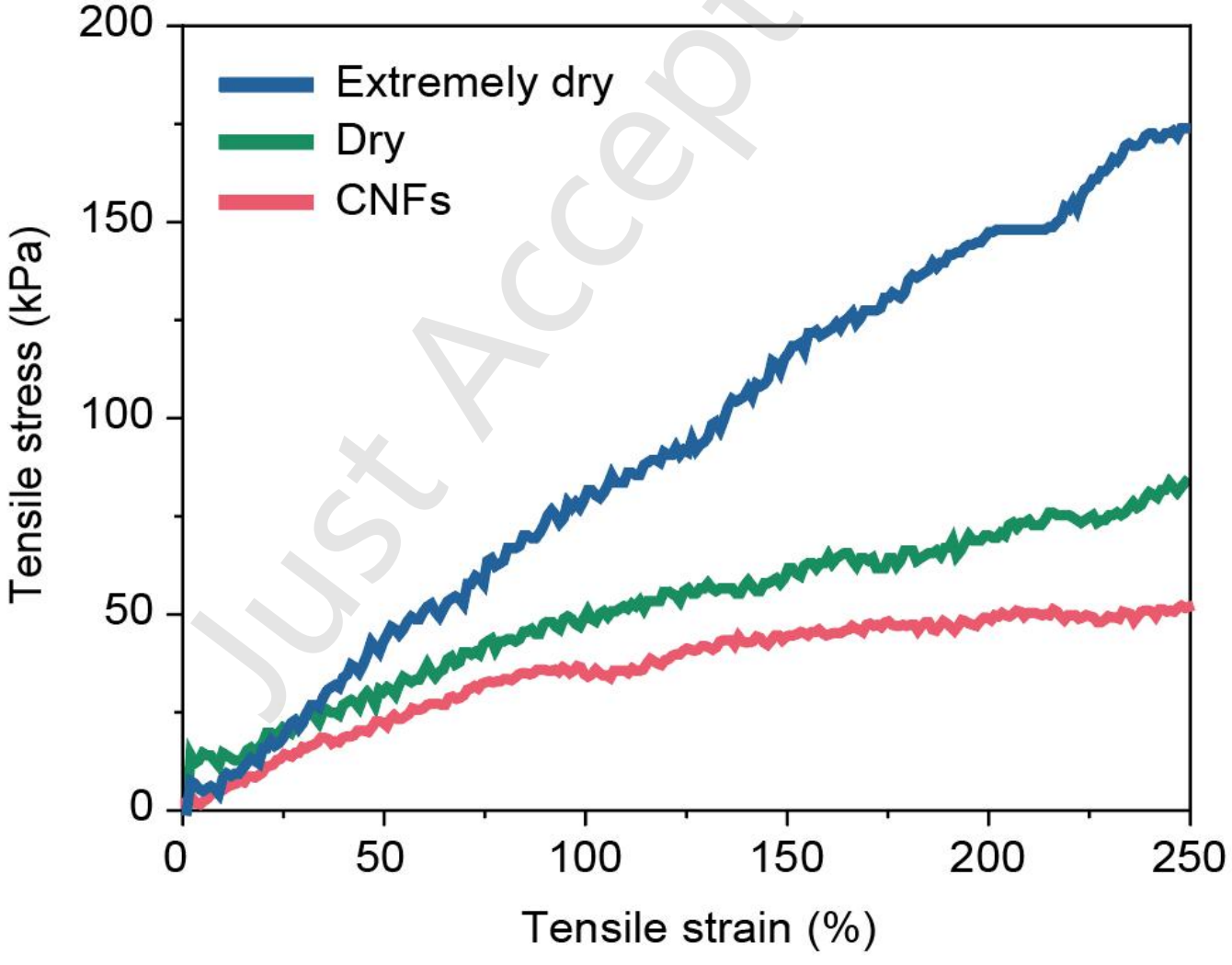

Figure S5 The stiffness of CNFs, dry and extremely dry porcine skin.

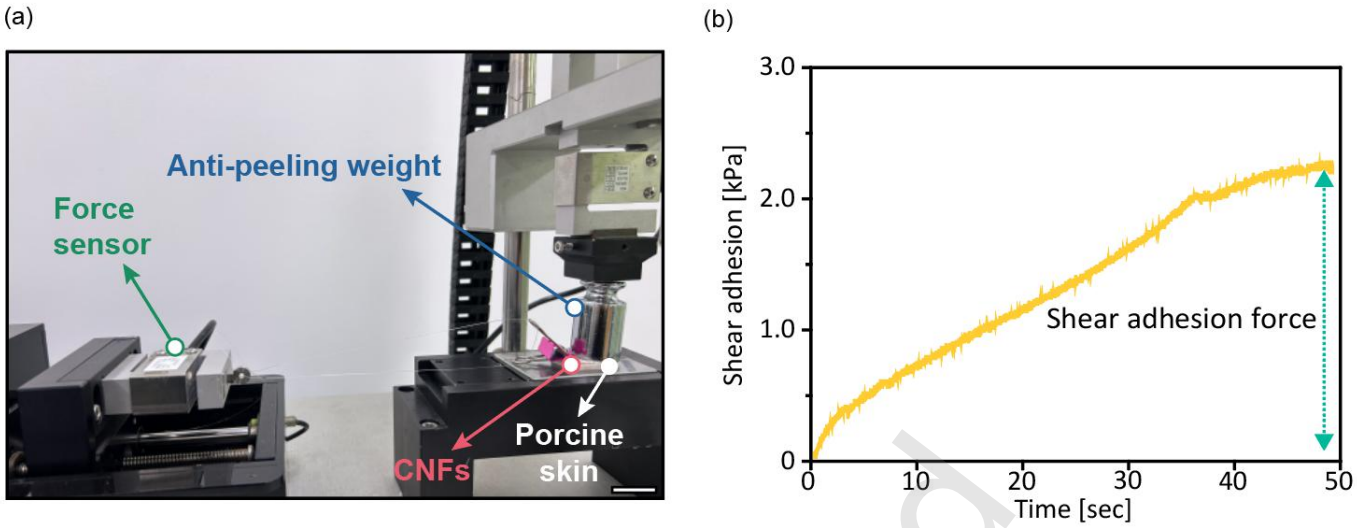

Figure S6 Setup for adhesion tests. Measurement of shear adhesion performance of the CNFs on porcine skin using custom-built equipment (scale: 1 cm). (b) Representative time-dependent profile of shear adhesion.

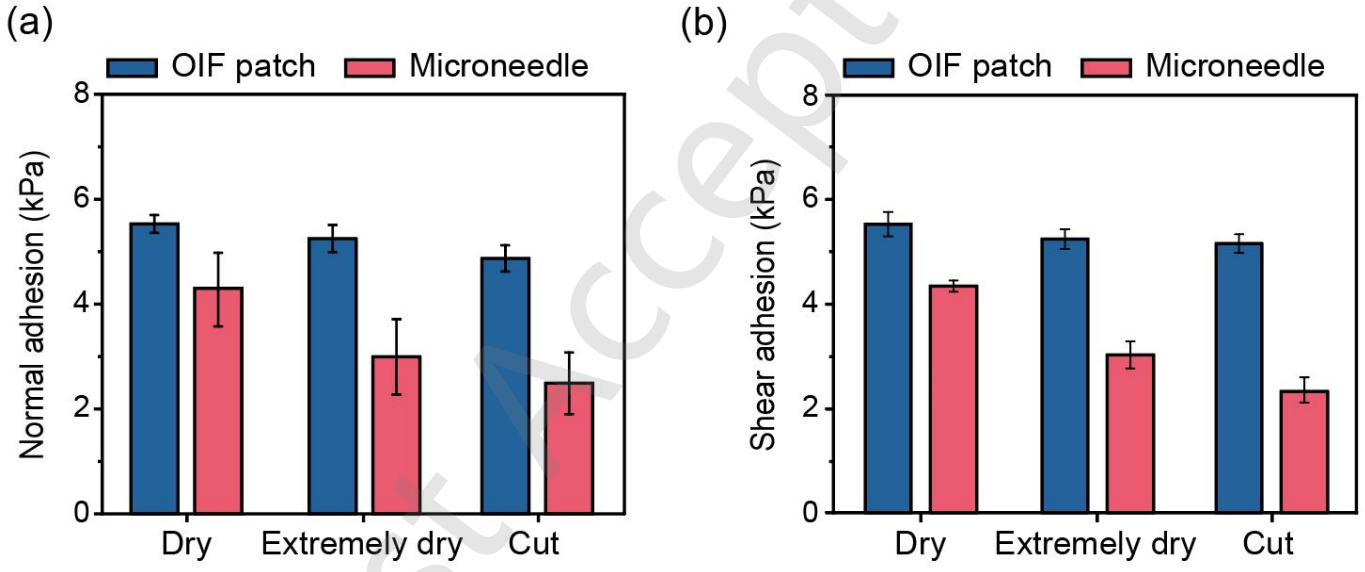

Figure S7 (a) Normal adhesion performance of OIF patch and microneedle on various skin conditions; n = 10. (b) Shear adhesion performance of OIF patch and microneedle on various skin conditions; n = 10.

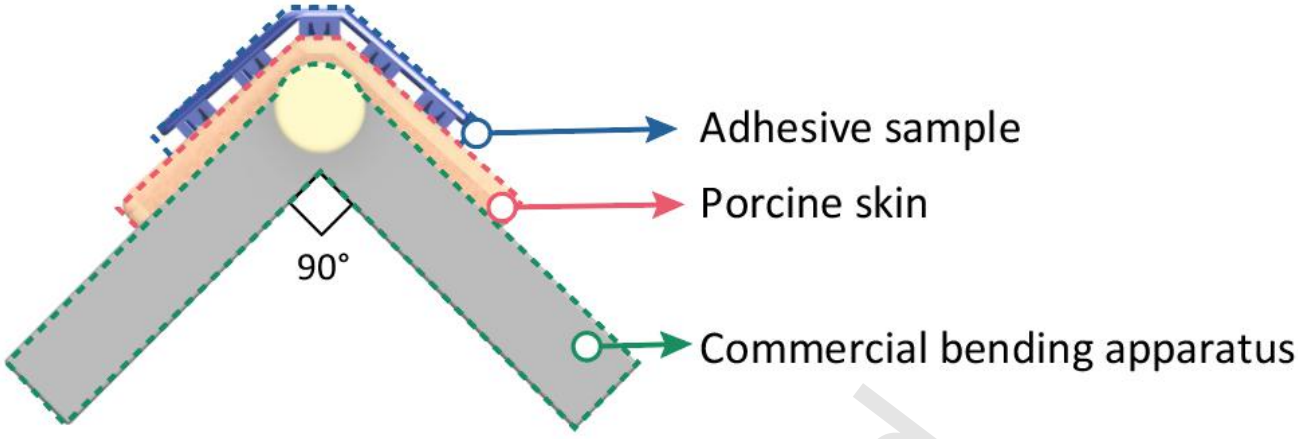

Figure S8 Schematic of the experimental setup for applying adhesive samples in a bending state using a commercial bending apparatus.

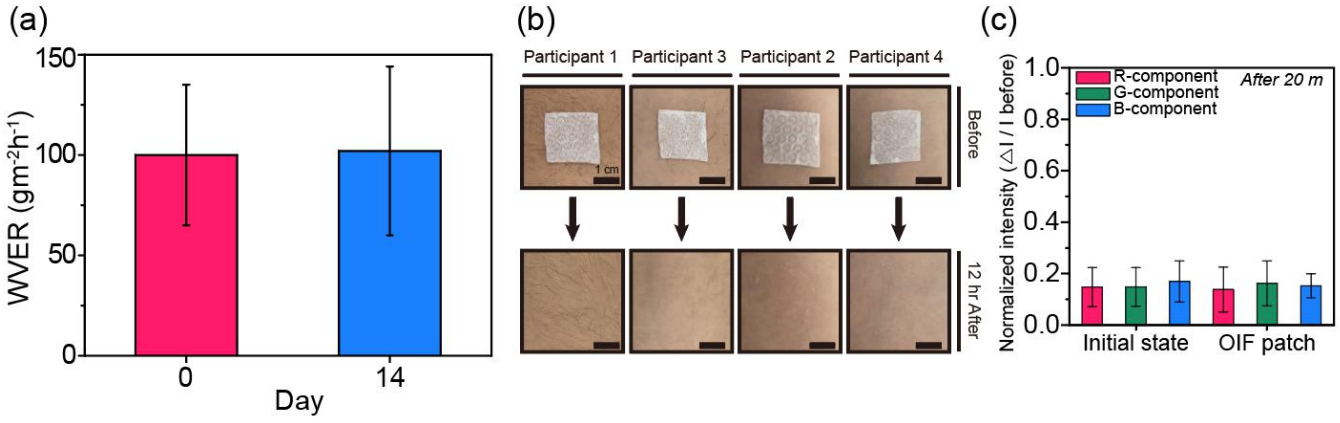

Figure S9 (a) Comparison of water vapor evaporation rate (WVER) before and after 14 days of OIF patch application (n = 5). (b) Representative skin images of subjects before and after OIF patch application (20 min) (n = 4). (c) Quantitative analysis of normalized RGB intensity of the skin before and after OIF patch application.

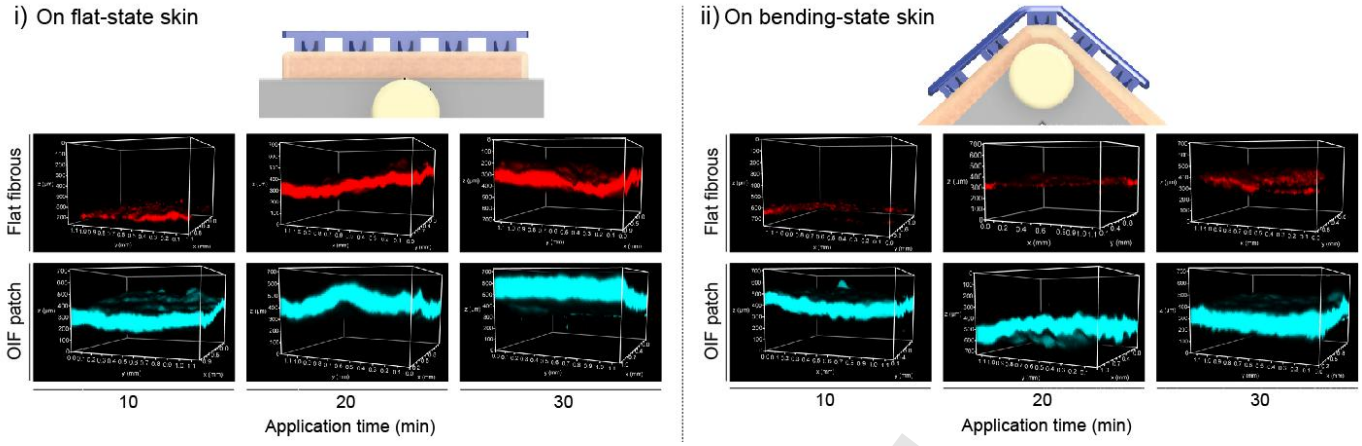

Figure S10 3D confocal microscopy analysis of fluorescent particles diffusion through porcine skin in (i) flat and (ii) bending states at various application times (10, 20, and 30 min).

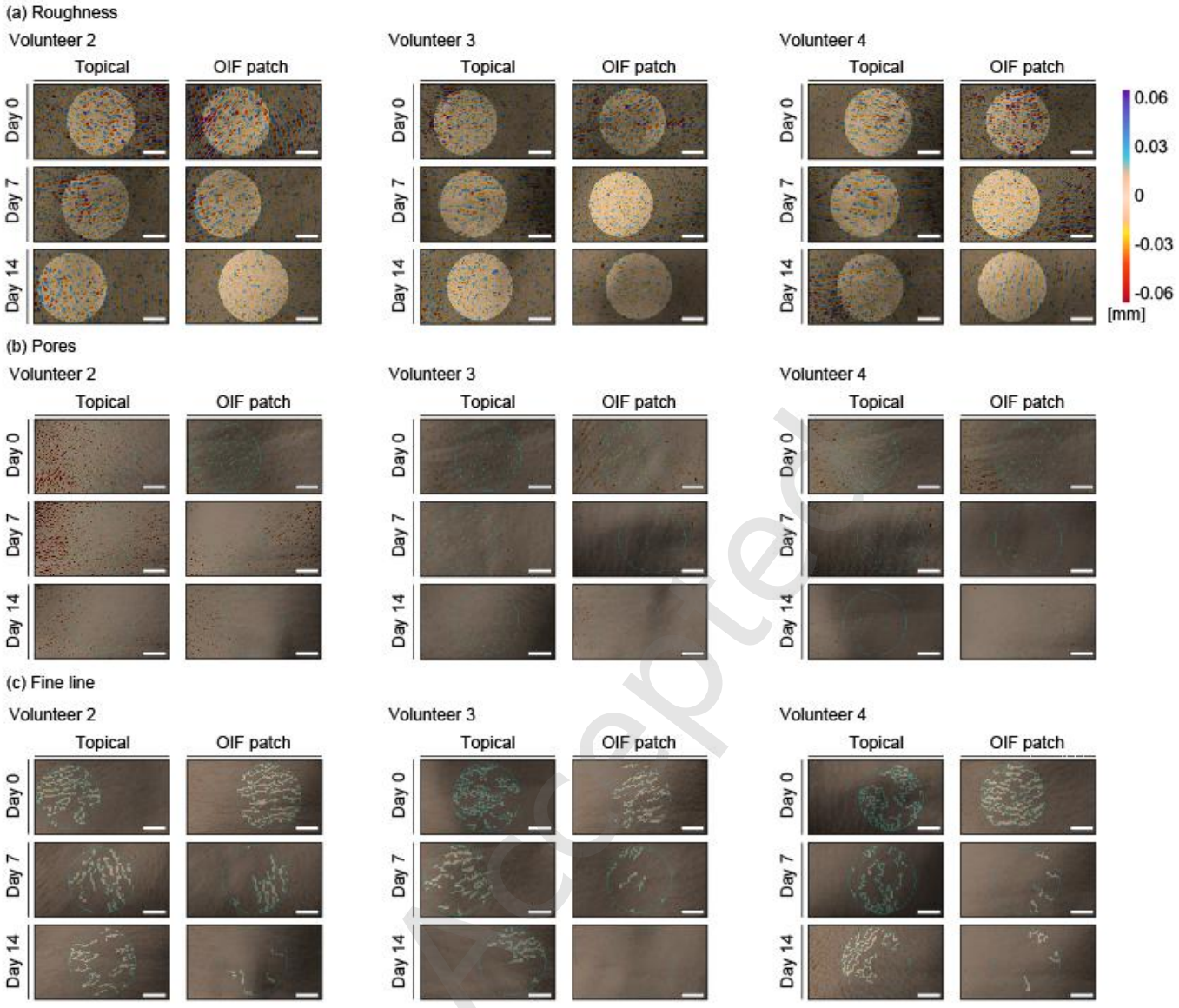

Figure S11 Representative images of (a) roughness, (b) pores, and (c) fine line of volunteers' skin with different delivery methods (topical, OIF patch) over varying application days (scale: 1 mm).

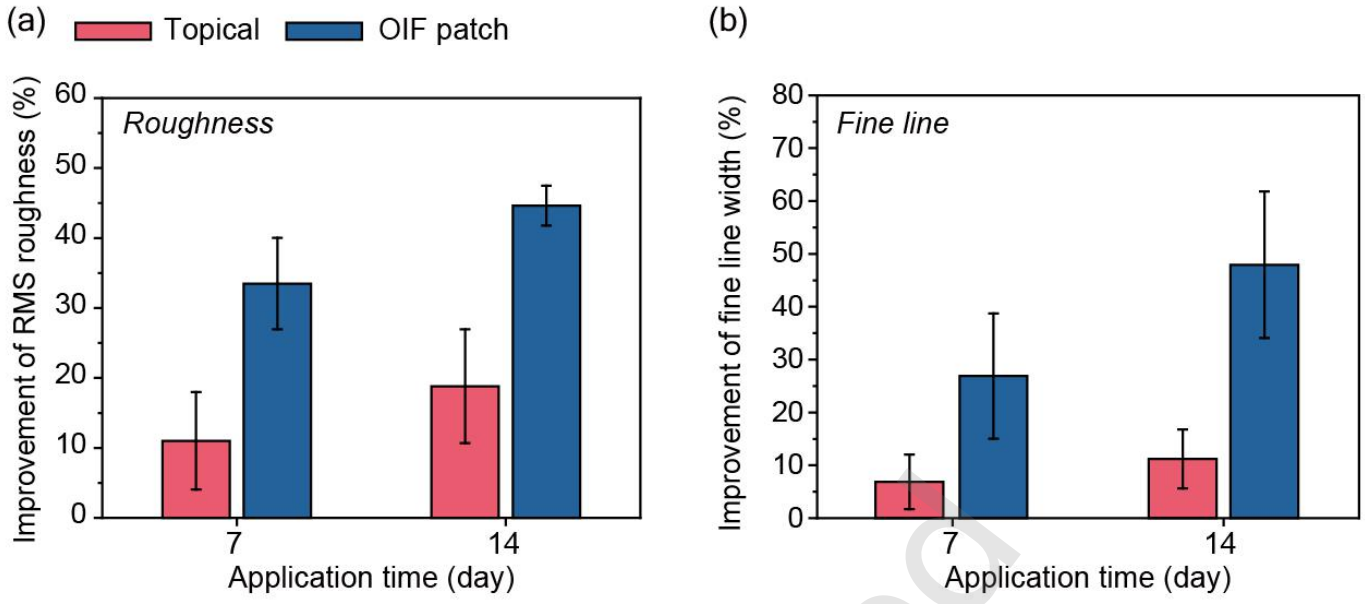

Figure S12 Changes in (a) root mean square of the roughness profile ordinate and (b) average width of fine lines; *n* = 16.

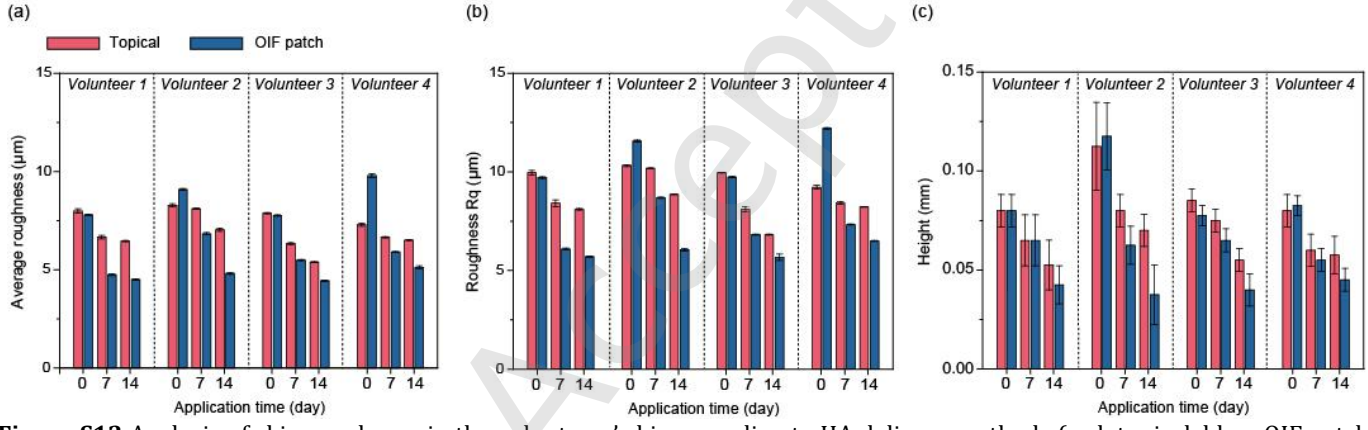

Figure S13 Analysis of skin roughness in the volunteers' skin according to HA delivery methods (red: topical, blue: OIF patch) at different application times (Day 0, Day 7, and Day 14). Changes in (a) the average roughness of all deviations from a straight line within the evaluation length, (b) the root mean square of the roughness profile ordinate, and (c) the height between the maximum and the minimum point of the profile; *n* = 16.

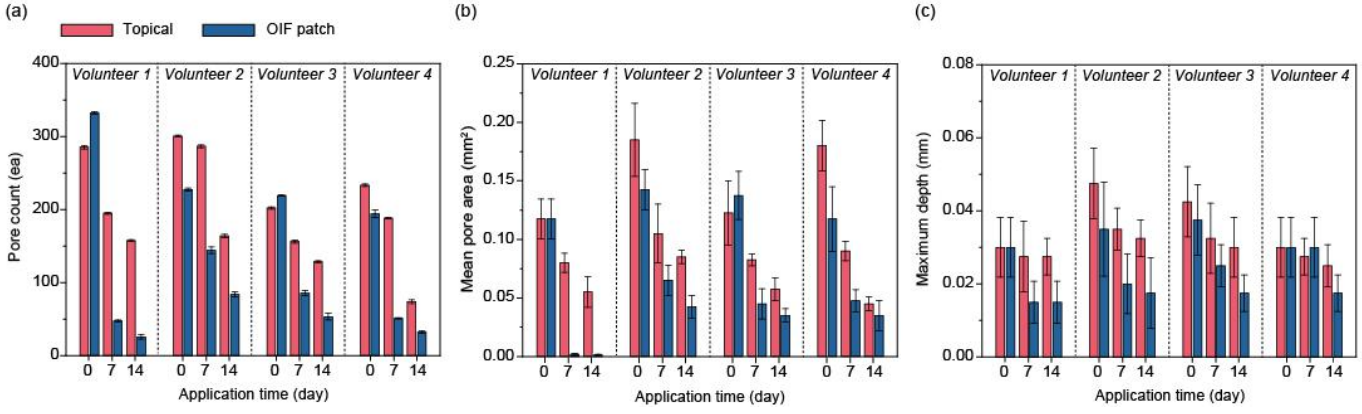

Figure S14 Analysis of pores in the volunteers' skin according to HA delivery methods (red: topical, blue: OIF patch) at different application times (Day 0, Day 7, and Day 14). Changes in (a) counts, (b) mean area, and (c) maximum depth of pores; n = 16.

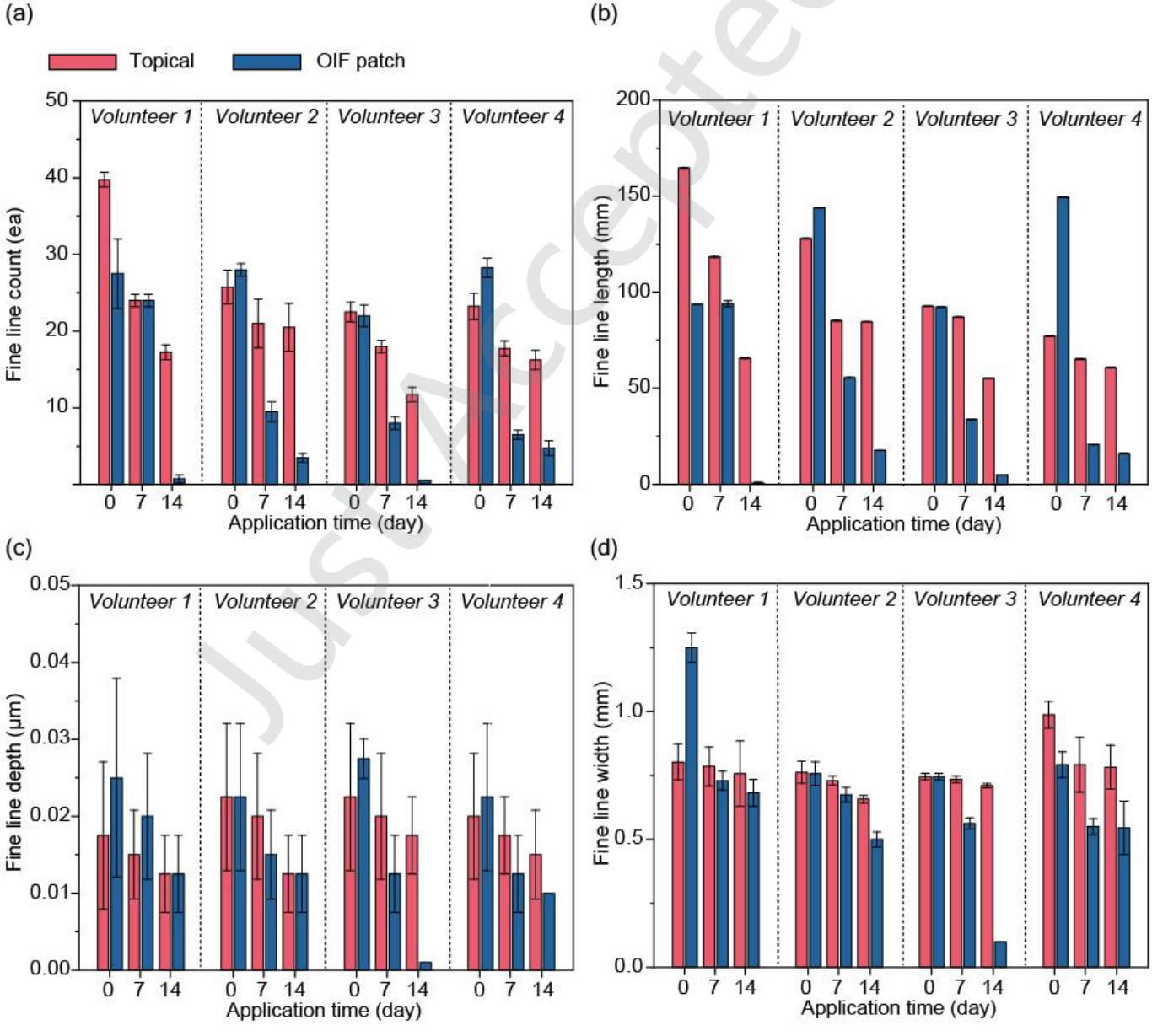

Figure S15 Analysis of fine lines in the volunteers' skin according to HA delivery methods (red: topical, blue: OIF patch) at different application times (Day 0, Day 7, and Day 14). Changes in (a) counts, (b) sum of lengths, (c) average depth, and (d)

average width of fine lines; n = 16.

Supplementary Note 1

Derivation of the adhesion for octopus-inspired suction cup (OISC)

Upon application of a preload of 5 kPa, the outer diameter of the octopus-inspired suction cup (OISC) after attachment (D''_{out}) increases relative to its initial undeformed diameter (D''_{out}). This deformation behavior was quantitatively analyzed using finite element method (FEM) simulations, which capture the structural response of the OISC geometry under compressive loading. Under wet conditions, the total adhesion stress (σ_{total}) generated by the OISC can be expressed as the sum of capillary stress ($\sigma_{capillary}$), suction stress ($\sigma_{suction}$), and viscous stress ($\sigma_{viscous}$), each scaled by the effective contact area of the structure.

$$\sigma_{total} = \sigma_{capillrary} + \sigma_{suction} + \sigma_{viscous} \tag{S1}$$

The capillary stress arises from the combined effects of Laplace pressure and surface tension acting on a unit area and is given by:

$$\sigma_{capillrary} = \left[\frac{\pi\cdot(D''_{out}{}^2 - D''_{in}{}^2)}{4}\cdot\gamma\left(\frac{\cos\vartheta_1+\cos\vartheta_2}{h}\right) + l\cdot\gamma\right]\cdot n \tag{S2}$$

Where γ is the surface tension of HA depends on concentration, ϑ_1 is the contact angle of cellulose nanofiber and HA, ϑ_2 is the contact angle of HA on the engaged substrate, h is the liquid gap, l is the outer circumference, and n is the number of structures. The suction stress generated under wet conditions is expressed as:

$$\sigma_{suction} = \left[\frac{P_0\pi D''_{in}{}^2}{4}\right]\cdot n \tag{S3}$$

Where P_0 corresponds to atmospheric pressure (~101.3 kPa), and D_{in}'' is the inner diameter of the structure after deformation induced by preload application.

Because the viscosity of HA induces structural deformation and alters the internal chamber volume, the suction stress was further refined by incorporating the volumetric change ratio, defined as $\varepsilon = (V_0 - V_1)/V_0$, where V_0 and V_1 are the initial and deformed chamber volumes, respectively. The viscosity-dependent suction stress is therefore described as:

$$\sigma_{suction} = \left[\frac{P_0\pi D''_{in}{}^2\epsilon}{4}\right]\cdot n \tag{S4}$$

In addition, the viscous stress increases linearly with the viscosity of HA and can be expressed as:

$$\sigma_{viscous} = \left[\frac{6v\cdot\eta\cdot\pi}{h}\cdot\frac{(D''_{out}{}^2 - D''_{in}{}^2)}{4}\right]\cdot\mathrm{n} \tag{S5}$$

Where v is the sliding velocity and η denotes the viscosity of HA. By combining all contributing stress components, the total wet adhesion stress can be summarized as:

$$\sigma_{total} = \left[\frac{P_0\pi D''_{in}{}^2\epsilon}{4} + \frac{\pi(D''_{out}{}^2 - D''_{in}{}^2)}{4}\cdot\left(\frac{6v\cdot\eta}{h} + \gamma\left(\frac{\cos\vartheta_1+\cos\vartheta_2}{h}\right) + l\cdot\gamma\right)\right]\cdot\mathrm{n} \tag{S6}$$